

https://dspace.org/

Ab-initio study of elastic and structural properties of layered nitride materials

Manyali, George Simiyu

2012-06-14
http://hdl.handle.net/10539/11480

Downloaded from a DSpace repository. https://dspace.org/

AB-INITIO STUDY OF ELASTIC AND STRUCTURAL PROPERTIES OF LAYERED NITRIDE MATERIALS

George Simiyu Manyali

A dissertation submitted to the Faculty of Science, University of the Witwatersrand, Johannesburg, in fulfilment of the requirements for the degree of Master of Science.

.

Johannesburg, February 2012.

Declaration

I declare that this dissertation is my own, unaided work. It is being submitted for the degree of Master of Science by Dissertation in the University of Witwatersrand, Johannesburg. It has not been submitted before for any degree or examination in any other University.

_____

(Signature of the candidate)

_____day of _____2012

Abstract

Layered nitride materials in the form of Carbon nitride (C_3N_4) was speculated nearly 22 years ago. It has various structural forms ranging from layered graphitic to superhard structures. Using first principles calculations based on density functional theory, the structural and elastic properties of these phases are determined. Elastic constants, bulk and shear moduli of cubic phases are compared to that of diamond. From the work it is evident that, although the compressibility of some of the superhard phases may be better than diamond, the shear modulus indicates that C_3N_4 is not harder than diamond in contrast to what has been speculated ealier. The graphitic hexagonal, rhombohedral as well orthorhombic phases are soft as indicated by their bulk and shear moduli, which are similar to that of graphite. Other elastic properties such as the Young modulus and Poisson's ratio as well as the Raman and infrared vibrational frequencies are also presented in this dissertation.

Dedication

To mum Topisita Nakhumicha and dad Eric Manyali

To my wife Pamela and our son Nicola Chetty.

Acknowledgement

I would like to express my deep gratitude to my principal supervisor professor Alexander Quandt for his professional guidance throughout the research period. His wisdom, encouragement and willingness to assist at odd hours was a unique formula for the successful and timely completion of this work. Professor John Edward Lowther is thanked for his facilitation in writing this dissertation. His involvement in achieving the vision of the topic of research is greatly acknowledged. The financial support from the DST/NRF Centre of Excellence in Strong Materials is duly acknowledged. I also would like to express deep indebtedness to The African School Series on Electronic Structure Methods and Applications (ASESMA) workshop held at the African Institute for Mathematical Sciences (AIMS) in Muizenberg, South Africa in July 2010. Through this workshop, I got the bursary for my studies at the University of Witwatersrand, Johannesburg. Many thanks to the organizers of ASESMA2010 among them Professors; Nithya Chetty (University of Pretoria), Scandolo Sandro (The Abdus Salam International Centre for Theoretical Physics (ICTP), Italy), Richard Martin (Professor emeritus, University of Illinois) and Daniel Joubert (Professor in Physics at University of Witwatersrand). I thank Professor Richard Martin for his inspirational emails during the research period. Such words like " school and thesis research is hard for everyone! "....." " made me work hard in my studies.

Discussions with Mohammed Suleiman, Phineas Molepo, Isaac Motochi, Emily Aradi, Isaac Popola and many other postgraduate students (not mentioned here) at School of Physics is highly appreciated. Dr. George Amolo and Dr. Nicholas

Wambua are acknowledged for the professional guidance during the mentorship programme at Moi University, Kenya.

I am highly indebted to Dr. Robert Warmbier for his love and passion in reading and rereading several drafts of this dissertation. I thank him for his time we spent in discussing Computational Physics related problems. His assistance in writing Fortran codes is acknowledged as well.

The discussions with members of staff at the School of Physics is appreciated. Special thanks to Mr. Lesias Kotane, Professor Arthur Every, Dr. Zivayi Chiguvare and Dr. Bhekumusa Mathe.

Finally, I wish to thank the financial support, prayers and encouragement from our extended family of the late Philip Namonyo. Many thanks to my sisters; Coleta Nanjala “mama Lilian”, Maureen Nekesa “mama Respie”, Rose Nasimiyu “mama Ian”, Anne Nafula “mama Faith” , Lydia Naliaka “Biakhua”, Sussani Kisaka “madam” and Phoebe, my brothers Phily Namonyo “ kaka”, Eli Manyali “bwana ali” and Robert Manyali “Robo”.

Publications

1. G.S Manyali, J.E Lowther A. Quandt and R. Warmbier

   Ab-initio study of elastic properties of super hard and graphitic structures of C_3N_4 (submitted to PHYSICAL REVIEW B)

Contents

Declaration i

Abstract ii

Dedication iii

Acknowledgements iv

Publications vi

List of figures x

List of table xiii

List of Symbols and Abbreviations xvi

1 General Introduction 1

1.1 Experimental and Theoretical Ways of Estimating Hardness 2

1.2 Brief description of light elements 4

1.2.1 Carbon, Nitrogen and Boron 5

1.3 Super-hard Materials 6

1.4 Motivation 7

1.5 Research Objectives 7

1.6 Thesis Scope and Outline 8

2 Layered Carbon Nitride (C_3N_4) 9

2.1 Introduction 9

2.2 Super hard and precursor phases of C_3N_4 11

2.2.1 Cubic carbon nitride (ZB-C_3N_4) with defective zinc-blende structure 11

2.2.2 Cubic carbon nitride (c-C_3N_4) 12

2.2.3 Cubic spinel carbon nitride (s-C_3N_4) 12

2.3 Graphite-like carbon nitride (g-C_3N_4) 14

3 Theory of the Elastic constants of Materials 16

4 Theoretical Framework 21

4.1 Introduction 21

4.2 Many-body problem 22

4.3 Hartree-Fock Approximation [HF] 23

4.4 Density Functional Theory (DFT) 25

4.4.1 The Hohenberg-Kohn Theorem 26

4.4.2 The Kohn-Sham Equations 28

4.5 The Local Density Approximation (LDA) 31

4.6 Generalized gradient approximation (GGA) 31

4.7 Pseudopotentials 32

4.8 K-points 33

5 Computational Details **34**

5.1 Introduction 34

5.2 Vienna Ab-Initio Simulation Package (VASP) 35

5.3 Quantum ESPRESSO (QE) 36

5.4 Equation of states 37

5.5 Phonon frequency 38

6 Results and Discussion **40**

6.1 Ground state properties 40

6.2 Elastic constants 42

6.3 Elastic moduli 44

6.4 Covalent Bonds 51

6.5 Effect of Hydrostatic Pressure 54

6.6 Effect of pressure on elastic constants 54

6.7 Vibrational Frequencies 57

7 Conclusions **72**

7.1 Recommendation for Further Work 73

Appendices **80**

Conferences and Workshops **81**

Bibliography **81**

List of Figures

2.1 The crystalline structure model of unit cell of defective zinc-blende-C_3N_4.The brown spheres represent carbon atoms, and the grey spheres represent nitrogen atoms. 11

2.2 The crystalline structure model of one unit cell of cubic-C_3N_4.The brown spheres represent carbon atoms, and the grey spheres represent nitrogen atoms. 13

2.3 The crystalline structure model of one unit cell of cubic spinel-C_3N_4. The brown spheres represent carbon atoms, and the grey spheres represent nitrogen atoms. 13

2.4 Graphitic sheet of C_3N_4 within hexagonal super structures (2x2 cells). The brown spheres represent carbon atoms, and the grey spheres represent nitrogen atoms. 14

2.5 Graphitic sheet of C_3N_4 within rhombohedral structures (2x2 cells). The brown spheres represent carbon atoms, and the grey spheres represent nitrogen atoms. 15

2.6 Graphitic sheet of C_3N_4 within orthorhombic structures (2x2 cells). The brown spheres represent carbon atoms and the grey spheres represent nitrogen atoms. 15

5.1 The first Brillouin zone of the two dimensional graphite reciprocal lattice. The gamma point (wave vector k=0) lies at the center of the Brillouin zone. k1=k2=k3 are high symmetry points, while a1 and a2 are reciprocal lattice vectors. 39

6.1 Volume - pressure relationship of defective zinc-blende-C_3N_4. . . . 55

6.2 Total energy - pressure relationship in defective zinc-blende-C_3N_4. . 55

6.3 Bulk modulus, shear modulus and the three independent elastic constants; C_{11}, C_{12}, C_{44} as of C_3N_4 in defective zinc-blende structure. . 56

6.4 Calculated vibrational spectra of defect zinc-blende C_3N_4. The contributions of carbon and nitrogen atoms to the relative amplitudes of each vibrational frequencies are labeled in colour. 60

6.5 Vibrational spectra of cubic phase of C_3N_4. The contributions of carbon and nitrogen atoms to the relative amplitudes of each vibrational frequencies are labeled in colour. 62

6.6 Calculated vibrational frequencies of cubic-spinel phase of C_3N_4. The contributions of carbon and nitrogen atoms to the relative amplitudes of each vibrational frequencies are labeled in colour. . . . 64

6.7 The vibrational spectrum of graphitic C_3N_4 in hexagonal structure. The contributions of carbon and nitrogen atoms to the relative amplitudes of each vibrational frequencies are labeled in colour. Figures (a) and (b) show frequencies below and above 1000 cm^{-1} respectively. 68

6.8 The vibrational spectra of C_3N_4 in rhombohedral structure . The contributions of carbon and nitrogen atoms to the relative amplitudes of each vibrational frequencies are labeled in colour. 69

6.9 The vibration frequencies of C_3N_4 in orthorhombic structure. The contributions of carbon and nitrogen atoms to the relative amplitudes of each vibrational frequencies are labeled in colour. 71

7.1 Total energy versus kpoints for defect zinc-blende-C_3N_4. 74

7.2 The charge distribution in (a) defective zinc-blende-C_3N_4, (b) cubic-C_3N_4. 78

7.3 The charge distribution in (a) cubic spinel-C_3N_4(b) g-C_3N_4 (hexagonal) (c) g-C_3N_4 (rhombohedral) (d) g-C_3N_4 (orthorhombic). 79

List of Tables

6.1 The space groups of eight crystals structures and calculated first principles total energy in (eV), bulk modulus in (GPa), derivative of bulk modulus and equilibrium volume in ($Å^3$) obtained using Birch equation of state. 41

6.2 Calculated zero pressure elastic constants C_{ij} (GPa) for various C_3N_4 phases, diamond and graphite. 43

6.3 First principles elastic bulk modulus, shear modulus Young's modulus (all in GPa) and Poisson's ratio are presented. 50

6.4 Equilibrium lattice parameters (a, b and c), bond lengths and bond angles of diamond and six phases of C_3N_4 at ground state. Lattice parameters and bond length are in Å, while bond angles are given in degrees. 52

6.5 Calculated phonon frequencies of defective zinc-blende C_3N_4 with symmetry assignments (using VASP and Quantum ESPRESSO (QE)). The frequencies are given in cm^{-1}. 61

6.6 Characters of the irreducible representations of point group T_d of C_3N_4 in a defect zinc-blende, cubic and spinel type of structures. The T_d group consist of the identity E, four threefold rotation axes C_3 (eight elements), three twofold axes C_2 (three elements), six reflection plane S_d(six elements) and three fourfold rotation-reflection axes (six elements). Each row in this table is an irreducible representation of the group. 61

6.7 Calculated phonon frequencies of cubic C_3N_4 with symmetry assignments. The frequencies are given in cm^{-1}. 63

6.8 Calculated phonon frequencies of cubic spinel C_3N_4, with tentative symmetry assignments. The frequencies are given in cm^{-1} and imaginary modes are presented as i. 65

6.9 The full character table of the irreducible representations of point group C_{3h} for graphitic C_3N_4 in hexagonal structure. Each row in this table is an irreducible representation of the group. 66

6.10 Calculated vibrational frequencies of graphitic-C_3N_4, space group P_{6m2} with tentative symmetry assignments. The frequencies are given in cm^{-1}. 67

6.11 Characters of the irreducible representations of point group C_3v for rhombohedral structure of C_3N_4. The A modes are nondegenerate while E modes are doubly degenerate. 69

6.12 Calculated phonon frequencies of rhombohedral C_3N_4 using VASP. The frequencies are given in cm^{-1}. 70

6.13 Calculated phonon frequencies of Orthorhombic C_3N_4 using VASP. The frequencies are given in cm^{-1} and imaginary modes are presented as i. 71

7.1 Bulk modulus B (GPa) obtained by empirical method. 76

7.2 Hierarchy of hardness. 76

7.3 Characters of the irreducible representations of point group O_h(m-3m) corresponding to diamond. 77

7.4 Characters of the irreducible representations of point group D_3h (-62m) corresponding to graphite. 77

List of Symbols and Abbreviations

Å	Angstrom
B	Bulk modulus
B_V	Voigt bulk modulus
G_V	Voigt shear modulus
B_R	Reuss bulk modulus
G_R	Reuss shear modulus
B'	Derivative of bulk modulus
C-C	Carbon-carbon covalent bond
C-N	Carbon-nitrogen covalent bond
DFT	Density Functional Theory
LDA	Local density approximation
N-N	Nitrogen-nitrogen bond
UP-PP	ultra-soft Vanderbilt pseudopotentials
VASP	Vienna *ab initio* simulation package
u	Atomic mass unit
Y	Young's Modulus

Chapter 1

General Introduction

The demand of novel materials is the driving force behind material science in the 21^{st} century. The researcher's dream is to design new materials which suit particular industrial applications. One of the cheapest and easiest way of predicting new materials is by first principles calculations. The idea behind first principles, also known as *ab-initio*, calculation is to apply the basic laws of Physics to identify the composition of materials. Materials are made of atoms as building units. The atoms themselves consist of electrons. The behavior of a material is predicted by carrying out electronic structure calculations. The success of first principles calculations in predicting new materials and offering in-depth explanation of observations made in experiment can be attributed to intensive and extensive research in the field of condensed matter. Various theories have been developed, starting from Hartree in the 1930s to the popular and most celebrated framework of modern density functional theory. The other reason for the success of *ab-initio* based Physics is the rapid development of computer technology. However, it is also important to men-

tion that predictions made by *ab-initio* calculations are more useful when backed up by experimental synthesis of the predicted material.

The scientific and technological developments being witnessed today in machining and cutting industries require the use of wear resistant tools that are able to cut, drill or polish other surfaces. Traditionally, diamond has been the preferred candidate for such abrasive tools. Some of the fascinating properties that make diamond attractive for industrial application are high heat conductivity, a wide band gap, high mobility of electrons and holes and high hardness [1]. Diamond is the hardest known material on the earth today. The measured bulk modulus of diamond is 442 GPa, while its shear modulus and density are 553 GPa and 3515 kgm^{-3} respectively.

1.1 Experimental and Theoretical Ways of Estimating Hardness

The choice of materials for industrial applications depends on a variety of salient features exhibited by the material. Among those properties, the hardness of the material of formidable importance. Hardness is defined as the resistance of the material to local deformations [2] and it mainly depends on defects, pressure, temperature and dislocation. Deformation can be introduced through cutting, scratching, indentation or bending. Some old methods for measuring hardness include

1. Mohs Hardness Test [3]: This is one of the oldest ways of measuring hardness. The method was devised by the German mineralogist Friedrich Mohs in

1812. The Mohs hardness test involves observing whether a materials surface is scratched by another substance of known or defined hardness.

2. Brinell Hardness Test [4]: The Brinell test uses a desktop machine to apply a specified load to a hardened sphere of a specified diameter.

3. The Rockwell Hardness test also uses a machine to apply a specific load and then measure the depth of the resulting impression. The indenter may either be a steel ball of some specified diameter or a spherical diamond-tipped cone of 120 angle and 0.2 mm tip radius, called a brale.

4. Vickers and Knoop Microhardness Tests: The Vickers and Knoop Hardness Tests, are modifications of the Brinell test and are used to measure the hardness of thin film coatings or the surface hardness of case-hardened parts. With these tests, a small diamond pyramid is pressed into the sample under loads that are smaller than those used in the Brinell test. The difference between the Vickers and the Knoop Tests is simply the shape of the diamond pyramid indenter. The Vickers test uses a square pyramidal indenter which is prone to crack brittle materials. Consequently, the Knoop test using a rhombic-based (diagonal ratio 7.114:1) pyramidal indenter which produces longer but shallower indentations.

The theoretical methods for estimating hardness of materials involve the calculation of bulk moduli and shear moduli [5, 6]. The bulk modulus measures the resistance to the change in volume of solids while the shear modulu defines the resistance to reversible deformation upon shape change [2]. An empirical model to determine

bulk moduli of covalent solids such as C and Si is given by

$$B = \frac{(19.71 - 2.20\lambda)}{d^{3.5}} \tag{1.1}$$

In this case, the bulk modulus B is inversely proportional to the bond length d. The bulk modulus and the bond length are given in the units of Mbar and Å respectively. The ionicity of the compound is represented by λ. Silicon and other group IV homo-polar semiconductors have λ=0, while zinc-blende solids in groups III to V in periodic table has ionicity factor λ=1. Other heteropolar elements in group II-VI with zinc-blende structure have λ=2. According to this model, there are two essential properties that a hard material must have, low ionicity and short bond length.

It has been argued that the shear modulus correlates well with the hardness [7], and can hence be relied upon in prediction of hardness. Faming *et al* [8] proposed a semi empirical method for estimating hardness. Their method is based on the idea that the hardness of a covalent crystal is intrinsic and equivalent to the sum of the resistance to the indenter of each bond per unit area. We will see that the theoretical methods of estimating hardness produce results, which are comparable to experiments.

1.2 Brief description of light elements

Most of the light elements have the number of protons equal to number of neutrons. Good examples are hydrogen $^{2}_{1}$H, helium $^{4}_{2}$He , carbon $^{12}_{6}$C, nitrogen $^{14}_{7}$N and oxygen

$^{16}_{8}$O. Boron $^{10}_{5}$B is also regarded as a light element. Each of the elements mentioned above has its specific technological application. Boron, carbon and nitrogen belonging to group III, IV and V and form ultra-hard materials when bonded among themselves, e.g boron nitride (BN) and carbon nitride (CN) compounds. Carbon and nitrogen introduced in interstitial sites of 3d transition elements (vanadium, titanium etc.), form compounds that are hard and have wide industrial applications. Brief descriptions of their fundamental chemical properties are given for carbon, boron and nitrogen.

1.2.1 Carbon, Nitrogen and Boron

Carbon has the electronic configuration $1s^2 2s^2 2p^2$ and atomic mass of 12.011u. The core consists of 1s electrons while the other four electrons are valence electrons. The valence electrons of carbon form various types of bondings, sometimes with metal atoms occupying the holes in the resulting carbon framework. The bonding can be classified into three major forms, which correspond to valence orbital hybridizations sp^3, sp^2, and sp^1 [1]. Their formation is of great scientific and technological interest: the resulting structures such as diverse as the well known soft graphite, ultra-hard diamond and cage-like fullerenes. Natural graphite occurs in hexagonal and rhombohedral structures. Those two forms of graphite differ in the arrangement of the carbon planes. The hexagonal structure has an *AB* stacking, while the rhombohedral structure has an *ABC* stacking. Graphite is technologically useful as a dry lubricant, as moderator in nuclear power plants, in medical surgery and as strong heat resistant carbon fibre. Graphite is also interesting for graphite-

diamond studies because of its peculiar properties i.e. the existence of two types of interatomic bonding, weak Van der Waals bonds and strong sp^2 covalent bonds [9].

Nitrogen is a nonmetal element which has atomic number of seven and atomic mass 14.006u. The electronic configuration is $1s^2 2s^2 2p^3$. Boron on the other hand has one electron less than carbon. Its electronic configuration is $1s^2 2s^2 2p^1$. Boron is otherwise referred to as a frustrated element, because of its unique position between metals and insulators in the periodic table [10]. Overall, boron is lighter than carbon and nitrogen. It has an atomic mass of 10.811u.

1.3 Super-hard Materials

Boron, carbon and nitrogen form the atomic basis for the hardest materials known up to now [11]. Diamond was the first discovered super-hard material, followed by cubic boron nitride as second hardest material [1, 12]. A promising way to predict new super hard materials is by combining light elements in such a way, that the new compound adopts a diamond-like structure, with short interatomic bond lengths. Current research is focused on carbon nitride (C_3N_4), as a potential candidate for a hard super material. There have been various reports on electronic, elastic and optical properties of various phases of C_3N_4, but no detailed and systematic survey of this important material.

1.4 Motivation

Despite the fact that the prediction and synthesis of some C_3N_4 polymorphs has already been successful, there is great need to exhaustively determine the elastic and structural properties of a large number of possible polymorphs. The study of their elastic properties such as elastic constants provides fundamental information on how these materials behave under external strain. This kind of information helps us to understand thermal expansion, melting point, atomic bonding and their structural stability.

1.5 Research Objectives

The objectives of this study are;

1. To obtain the lattice parameters, bond length and bond angles of six example phases of C_3N_4.

2. To obtain equilibrium volume and ground state energies.

3. To obtain their elastic constants.

4. To obtain the bulk modulus, shear modulus, Young modulus and Poisson's ratio.

5. To investigate their vibration modes and other optical properties.

1.6 Thesis Scope and Outline

The aim of this study is to examine the structural, elastic and some optical properties for different phases of (layered) carbon nitride. The first principles calculations are carried out using the density functional theory formalism as implemented in VASP and Quantum ESPRESSO. These present dissertation has two major parts. In the first part, ground state properties are presented. These include the bulk modulus, shear modulus, interatomic distances, bond lengths, equilibrium volume and total energy. Elastic constants, Poisson's ratio and Young modulus are reported as well. The second part is devoted to vibrational frequencies calculated at the gamma point. Here the resulting infrared and Raman spectra are discussed in some detail.

To be more specific: in chapter 2, a detailed account of structural properties of various polymorphs of C_3N_4 are presented. Two distinct structures are highlighted, diamond-like and graphite-like structures. The super-hard phases of C_3N_4 have diamond-like structure, while precursor phases have graphitic structures. Next, theories of elastic constants are featured in chapter 3 with emphasis on the Voigt contracted notation of elastic coefficients. Then some background information on the density functional theory is given in chapter 4 and the Kohn-Sham equations and their numerical relations are summarized. Chapter 5 gives an overview of calculations carried out using VASP and Quantum ESPRESSO, while the main results are summarized in chapter 6. The conclusion and recommendations for future studies are presented in chapter 7.

Chapter 2

Layered Carbon Nitride (C_3N_4)

2.1 Introduction

The search for super hard materials has been going on for the past few decades. Focus has been directed to the synthesis of materials with extreme hardness or hardness very close to that of diamond. These new super hard materials are expected to have high bulk modulus, high thermal conductivity, spectral transmittance, microhardness exceeding 4000kg mm^{-2}, high refractive index, hole mobilities and high shear modulus [13, 14]. Compounds made of light elements such as boron, carbon and nitrogen [15] as well as heavy transition metals and their carbides, nitrides and oxide [16] are known to have extreme hardness, oxidation resistance and chemical inertness [17]. The demand for super-hard materials is on the increase, because of wide industrial applications such as cutting, drilling, grinding and polishing [18]. Superhard material are also used as heat sinks, radiation windows, speaker tweeters, mechanical bearing, surgical knifes and semiconductors [14]. Experimental

and theoretical research have indicated that carbon nitrides are possible candidates for super hard materials, since they exhibit short carbon-nitrogen (C-N) covalent bonds and bulk moduli comparable to that of diamond [19]. The first prediction of low compressibility solids was reported by Cohen in 1989 [5]. These authors proposed β-C_3N_4 (space group $P_{63/m}$), whose structure is based on β-Si_3N_4, with C substituting Si. Those prediction lead to intense theoretical research [20–25] and experimental [26–31] attempts to synthesis various phases of carbon nitride. It is worth noting that direct synthesis of three dimensional C_3N_4 is thermodynamically unfavored due to the high stability of N_2 [32]. It has been impossible to thoroughly characterize the nitrides, because the crystalline phases are usually embedded in an amorphous carbon nitride matrix [33]. Reference [34] reports success and limitations of some experimental characterization techniques applied in the synthesis of the C_3N_4 polymorph. X-ray diffraction, photo electron spectroscopy, nuclear magnetic resonance, back scattering and transmission electron spectroscopy are examples of experimental methods widely used in the characterization of hard materials. The proposed structures of the carbon nitrides can be viewed as candidates for low compressibility materials, or at least as precursors for super hard polymorph.

2.2 Super hard and precursor phases of C_3N_4

2.2.1 Cubic carbon nitride (ZB-C_3N_4) with defective zinc-blende structure

The defective zinc-blende structure (diamond structure with one atom less) belongs to space group $P_{43/m}$ and has been predicted to have cubic lattice constant of 3.41 Å [18]. The structure can be described as being derived from diamond structure by replacing some of the carbon atoms with nitrogen atoms [35]. ZB-C_3N_4 is a low compressibility material because of the tetrahedral formation of C-N covalent bonds as shown in figure 2.1. Each of the carbon atoms is bonded to four neighboring nitrogen atoms, while each nitrogen atom is bonded to three carbon atoms. This structure has been identified to be mechanically stable [36].

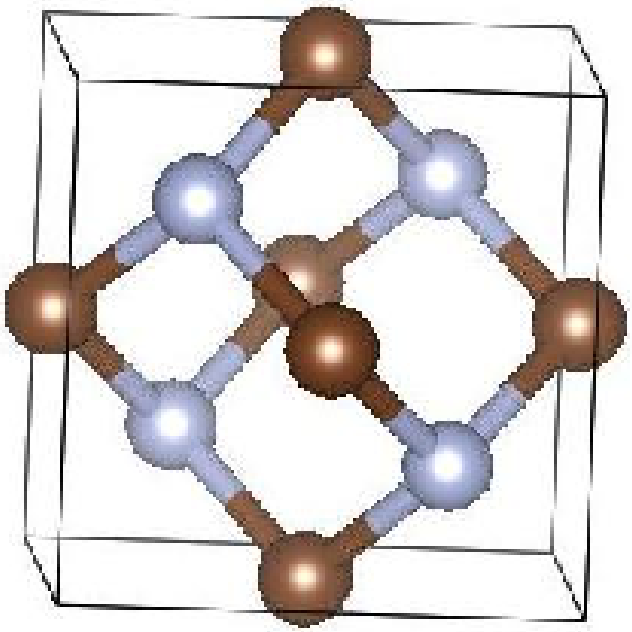


Figure 2.1 The crystalline structure model of unit cell of defective zinc-blende-C_3N_4.The brown spheres represent carbon atoms, and the grey spheres represent nitrogen atoms.

2.2.2 Cubic carbon nitride (c-C_3N_4)

The cubic-C_3N_4 (space group I_{43d}) is the hardest phase amongst the proposed C_3N_4 phases. It contains 28 atoms per the unit cell. The recent experimental work on the synthesis of the cubic phase shown in figure 2.2, demonstrated that the theoretical search for super hard material is not in vain. Graziella et al [37] synthesized c-C_3N_4 through a decomposition of commercial thiosemicarbazide powder under nitrogen flow at ambient pressure and 600 ^oC. The identified c-C_3N_4 with lattice constant of 3.16 Å and bulk modulus of 355 GPa could not be categorized in any known space group. Zinin et al [38] managed to synthesize new c-C_3N_4 with lattice constant 3.878 Å under high-pressure and high-temperature (HPHT) conditions. Again this new c-C_3N_4 phase could not be categorized in any known space group. For the two syntheses above, a well characterized graphitic phase was used as a precursor.

2.2.3 Cubic spinel carbon nitride (s-C_3N_4)

Search for nitrides with spinel structure came into focus immediately after the discovery of cubic silicon nitride (c-Si_3N_4) [39]. The c-Si_3N_4 has been reported to have a wide band gap of 3.45 eV appropriate for light emitting devices. Several other nitrides with similar spinel structure like Ge_3N_4, Ti_3N_4, Sn_3N_4, Zr_3N_4 and s-C_3N_4 were predicted [40–42]. The s-C_3N_4 structure belong to space group F_{d3m} and contains 56 atoms in the unit cell. This crystal structure has two kinds of binary systems, octahedral CN_6 whereby each carbon atom is coordinated with six nitrogen atoms, and tetrahedral CN_4 where each carbon has four neighboring nitrogen

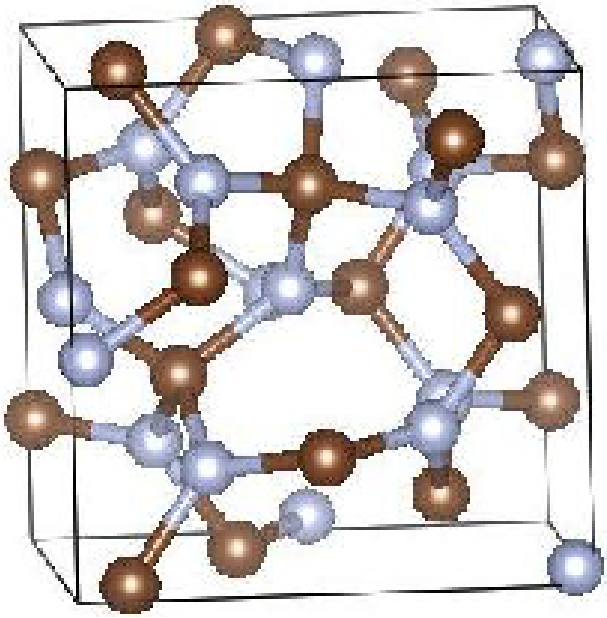


Figure 2.2 The crystalline structure model of one unit cell of cubic-C_3N_4.The brown spheres represent carbon atoms, and the grey spheres represent nitrogen atoms.

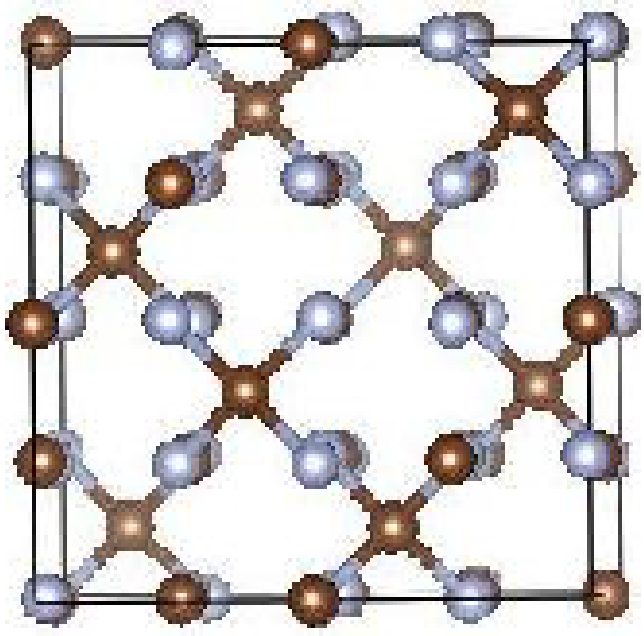


Figure 2.3 The crystalline structure model of one unit cell of cubic spinel-C_3N_4. The brown spheres represent carbon atoms, and the grey spheres represent nitrogen atoms.

atoms, as shown in figure 2.3.

2.3 Graphite-like carbon nitride (g-C_3N_4)

The successful synthesis of c-C_3N_4 under high-pressure, high-temperature conditions underscores the usefulness of graphitic-carbon nitride (g-C_3N_4) as precursors for super hard phases of carbon nitride. The atoms are arranged in such a way that each C atom is bonded with the three nearest N atoms, while two N atoms form bonds with three neighboring C atoms. The g-C_3N_4 structure has been predicted to be the energetically favorable and stable structure. A variety of graphitic structures has been proposed: Figure 2.4 shows a hexagonal structure (space group P_{6m2}) of g-C_3N_4 predicted by Teter and Hemley [20].

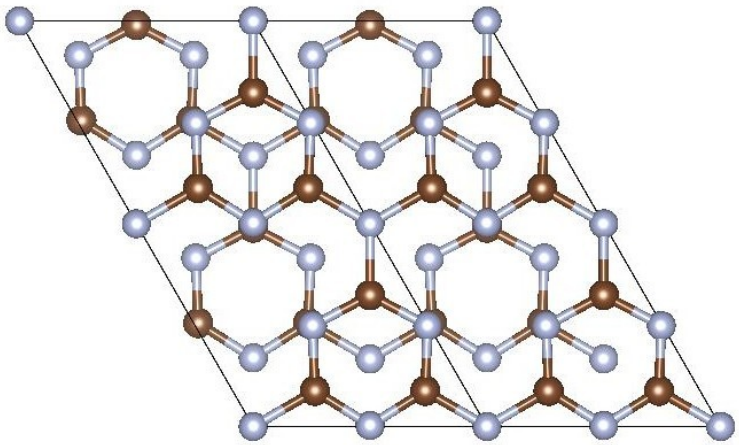


Figure 2.4 Graphitic sheet of C_3N_4 within hexagonal super structures (2x2 cells). The brown spheres represent carbon atoms, and the grey spheres represent nitrogen atoms.

Liu and Renata [25] proposed a defective graphitic carbon nitride (space group R_{3m}) with a rhombohedral structure shown in figure 2.5. This graphitic phase has ABCABC rhombohedral stacking ordering. Due to weak inter layer bonding, this structure was unlikely to form low compressibility material.

Alves *et al* [28] synthesized an orthorhombic g-C_3N_4. They classified the struc-

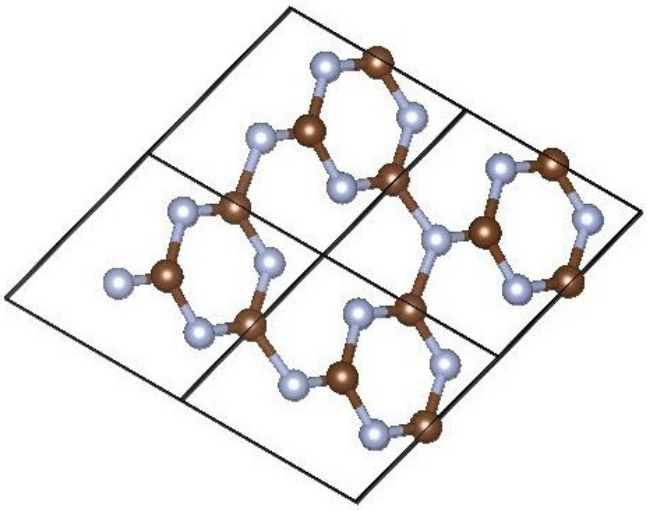


Figure 2.5 Graphitic sheet of C_3N_4 within rhombohedral structures (2x2 cells). The brown spheres represent carbon atoms, and the grey spheres represent nitrogen atoms.

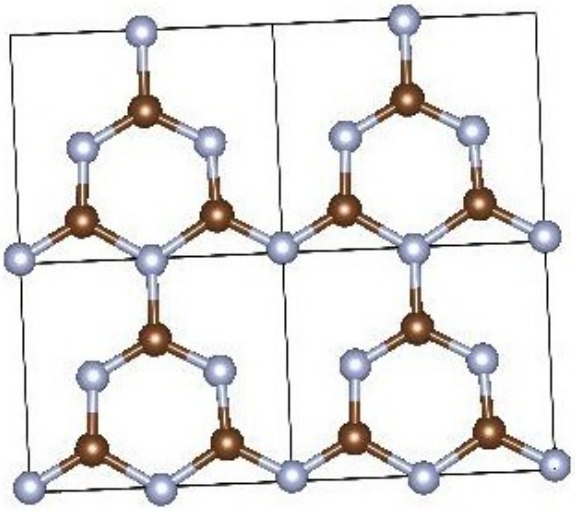


Figure 2.6 Graphitic sheet of C_3N_4 within orthorhombic structures (2x2 cells). The brown spheres represent carbon atoms and the grey spheres represent nitrogen atoms.

ture in two stacking orderings i.e AA and AB. The two orderings belong to the space group P_{2mm}. The AA ordered orthorhombic structure was reported to have lattice parameters a=4.1 Å, b=4.7 Å and c=3.2 Å while the AB stacking has lattice parameter a=4.1 Å, b=4.7 Å and c=6.4 Å.

Chapter 3

Theory of the Elastic constants of Materials

There are several methods proposed in the literature for determining the elastic constants of materials [43–48]. In this work, descriptions of the elastic constants of isotropic and anisotropic materials are highlighted. An isotropic material is characterized by material's properties, which are independent of the direction of the principal axis frame. For instance, an isotropic material will have the same stiffness, irrespective of the direction of an applied external force. Steel and aluminium are good examples of isotropic materials formed in nature. On the other hand an anisotropic material is a material, whose properties will depend on the direction of the applied force. Examples include graphite and carbon nitride. The anisotropy of a given material may become a great challenge in particular when determining the corresponding elastic constants (theoretically as well as experimental). In describing elastic constants, the material is subject to applied external forces (stress

tensors), which lead to deformations described by a strain tensor. The material under investigation is assumed to be homogeneous. Similarly the applied stress as well as resultant strain are also assumed to be uniform. The stress-strain relationship may be seen as some sort of generalized Hooke's laws. Hence, elastic constants in terms of such a generalized Hooke's law are given as

$$\sigma_{ij} = C_{ijkl}\varepsilon_{kl}, \tag{3.1}$$

where σ_{ij} is the stress tensor, ε_{kl} is the strain tensor and C_{ijkl} is the stiffness tensor. The labels i,j,k,l are 1,2,3, corresponding a system of axes fixed in space.

Inverting equation 3.1 produces a relationship, in which the strain is expressed in terms of stress as follows

$$\varepsilon_{ij} = S_{ijkl}\sigma_{kl}. \tag{3.2}$$

Here S_{ijkl} is the compliance tensor. The C_{ijkl} contains 81 elastic coefficients, which reduce to 21 independent elastic coefficients, due to symmetry [49].

The special symmetries of individual lattice structures further reduce the number of independent elastic coefficients. In the following, I use the so-called Voigt notation [50, 51] where the C_{ijkl} is reduced to a six by six matrix C_{ij} as a result of symmetry with i,j=1...6. The C_{ij} are categorized into four groups; the first group includes elastic constants along the main diagonals. The corresponding elastic constants C_{11}, C_{22} and C_{33} are called longitudinal elastic constants. The second category, which contains diagonal constants with i$\geq$4 comprises the so-called shear

elastic constants. The third category comprises C_{ij} with i≠j, and i,j<3. This group is known as off-diagonal constants. The fourth and last category is referred to as mixed elastic constants. This category has C_{ij} with i≤3 and j>3, e.g. C_{34}. A brief description of elastic coefficient matrices of selected crystal structures is given below.

Triclinic lattice structures have 21 independent elastic coefficients

$$C_{ij} = \begin{bmatrix} C_{11} & C_{12} & C_{13} & C_{14} & C_{15} & C_{16} \\ & C_{22} & C_{23} & C_{24} & C_{25} & C_{26} \\ & & C_{33} & C_{34} & C_{35} & C_{36} \\ & & & C_{44} & C_{45} & C_{46} \\ & & & & C_{55} & C_{56} \\ & & & & & C_{66} \end{bmatrix} \tag{3.3}$$

Due to symmetry, orthorhombic lattice structures have nine independent elastic constants.

$$C_{ij} = \begin{bmatrix} C_{11} & C_{12} & C_{13} & 0 & 0 & 0 \\ & C_{22} & C_{23} & 0 & 0 & 0 \\ & & C_{33} & 0 & 0 & 0 \\ & & & C_{44} & 0 & 0 \\ & & & & C_{55} & 0 \\ & & & & & C_{66} \end{bmatrix} \tag{3.4}$$

In these structures some coefficient elements are zero, while all elements along the main diagonal are nonzero. The trigonal, hexagonal and cubic lattice structures have six, five and three independent elastic constants respectively, as shown in matrices

3.5, 3.6 and 3.7. The C_{66} in both trigonal and hexagonal lattice structures appear as a combination of the C_{11} and C_{12} coefficients.

$$C_{ij} = \begin{bmatrix} C_{11} & C_{12} & C_{13} & C_{14} & -C_{15} & 0 \\ & C_{11} & C_{13} & -C_{14} & C_{25} & 0 \\ & & C_{33} & 0 & 0 & 0 \\ & & & C_{44} & 0 & C_{25} \\ & & & & C_{44} & -C_{14} \\ & & & & & \mathbf{\frac{1}{2}(C_{11} - C_{12})} \end{bmatrix} \tag{3.5}$$

$$C_{ij} = \begin{bmatrix} C_{11} & C_{12} & C_{13} & 0 & 0 & 0 \\ & C_{11} & C_{13} & 0 & 0 & 0 \\ & & C_{33} & 0 & 0 & 0 \\ & & & C_{44} & 0 & 0 \\ & & & & C_{44} & 0 \\ & & & & & \mathbf{\frac{1}{2}(C_{11} - C_{12})} \end{bmatrix} \tag{3.6}$$

$$C_{ij} = \begin{bmatrix} \mathbf{C_{11}} & C_{12} & C_{12} & 0 & 0 & 0 \\ & \mathbf{C_{11}} & C_{12} & 0 & 0 & 0 \\ & & \mathbf{C_{11}} & 0 & 0 & 0 \\ & & & \mathbf{C_{44}} & 0 & 0 \\ & & & & \mathbf{C_{44}} & 0 \\ & & & & & \mathbf{C_{44}} \end{bmatrix} \tag{3.7}$$

For cubic systems the longitudinal elastic constants are all equal, C_{11}=C_{22}=C_{33}.

Similarly, the three shear elastic constants are equal C_{44}=C_{55}=C_{66}. Many molecular crystals crystallize in low symmetry crystal structures such as triclinic, monoclinic and orthorhombic. The Voigt notation matrix of monoclinic lattice structure is

$$C_{ij} = \begin{bmatrix} C_{11} & C_{12} & C_{13} & 0 & C_{15} & 0 \\ & C_{22} & C_{23} & 0 & C_{25} & 0 \\ & & C_{33} & 0 & C_{35} & 0 \\ & & & C_{44} & 0 & C_{46} \\ & & & & C_{55} & 0 \\ & & & & & C_{66} \end{bmatrix} \tag{3.8}$$

In summary, the triclinic structures have the highest number of independent elastic constants, while cubic systems have the least. In practice, the calculation of elastic constants of cubic systems is the easiest because of their high symmetry.

Chapter 4

Theoretical Framework

4.1 Introduction

The properties of condensed matter and molecules are determined by the electrons and the nuclei. The study of electrons provides salient information about electronic, magnetic, optical and bulk properties of matter. Modern physics is faced with a challenge to develop computational methods that will accurately treat the interacting system of many electrons and nuclei. Furthermore, the calculation of electronic structures may be divided into ground state and excited state properties [52]. For the ground state features like the elastic properties, the charge density, equilibrium volumes and vibrational frequencies, may be obtained among many other interesting properties of matter. On the other hand, electronic excited states provide useful information about the optical properties etc. Various electronic structure methods have been developed in the past. The most prominent ones used for solid systems are Density Functional Theory (DFT) and Quantum Monte Carlo (QMC) [53–55].

DFT is a very reliable theory for predicting new materials, to confirm experimental discoveries, or to provide explanation of new phenomena observed in experimental work.

4.2 Many-body problem

A complete description of the quantum mechanical behavior of atoms requires detailed consideration of interactions between electrons and nuclei. For a system of N_e electrons and N_n nuclei, the non-relativistic time-independent Schrödinger equation is simply

$$H\Psi = E\Psi. \tag{4.1}$$

Ψ is the many-particle wavefunction and E is the total energy of the system. The many-particle wave function can either be symmetric or anti-symmetric. The symmetric case is describe as

$$\Psi = \Psi(r_1, \ldots, r_{N_e}) \tag{4.2}$$

while the anti-symmetric case is given by

$$\Psi = \Psi(r_1, \ldots, r_j r_i, \ldots, r_{N_e}) = -\Psi(r_1, \ldots, r_i r_j, \ldots, r_{N_e}) \tag{4.3}$$

The particles with half integer spins such as electrons are described by the anti-symmetric wave functions and they obey the Pauli exclusion principle. Such particles are termed fermions. The Pauli exclusion principle states that no two electrons can have the same set of quantum numbers, and electrons with the same spin cannot

occupy the same state simultaneously. Those particles whose wave functions are symmetric under particle interchange and have integral or zero intrinsic spin, are called bosons.

The Hamiltonian operator H in equation 4.1, can be written as

$$H = -\sum_{i=1}^{N_e} \frac{1}{2}\nabla_i^2 - \sum_{\alpha=1}^{N_n} \frac{1}{2M_\alpha}\nabla_\alpha^2 - \sum_{i=1}^{N_e}\sum_{\alpha=1}^{N_n} \frac{Z_\alpha}{\mid r_i - R_\alpha \mid} + \sum_{i=1}^{N_e}\sum_{j>i}^{N_e} \frac{1}{|r_i - r_j|} + \sum_{\alpha=1}^{N_n}\sum_{\beta>\alpha}^{N_n} \frac{Z_\alpha Z_\beta}{|R_\alpha - R_\beta|}. \tag{4.4}$$

M_α, Z_α and R_α are the mass, core charge and position of the nuclei, respectively. The position of electron is indicated as r_i. The first and second terms are the kinetic energies of the electrons and nuclei, respectively. The third term describes the Coulomb attraction between nuclei and electrons. The fourth and fifth terms describe the electron-electron and nucleus-nucleus Coulomb repulsion, respectively.

4.3 Hartree-Fock Approximation [HF]

The Hartree-Fock approximation is viewed as the basis or foundation for more accurate approximation involving correlation between electrons [56]. Within the HartreeFock approximation, the many body wave function of the system can be treated as a single Slater determinant of independent electrons which satisfies antisymmetry rule [57].

$$\phi = \frac{1}{\sqrt{N!}} \begin{vmatrix} \phi_1(x_1,\sigma_1) & \phi_1(x_2,\sigma_2) & ..... & \phi_1(x_N,\sigma_N) \\ \phi_2(x_1,\sigma_1) & \phi_2(x_2,\sigma_2) & ..... & \phi_2(x_N,\sigma_N) \\ ..... & ..... & & \\ ..... & ..... & & \\ \phi_N(x_1,\sigma_1) & \phi_N(x_2,\sigma_2) & ..... & \phi_N(x_N,\sigma_N) \end{vmatrix}.$$

where the $\phi_1(x_1,\sigma_1)$ are single particle spin orbitals.

Hartree-Fock theory provides an exact treatment of exchange correlation useful for calculations of molecules and larger N-body systems [52, 57–59]. The expectation value of the Hamiltonian with the wave function is described as

$$\begin{aligned} \langle\phi|\hat{H}|\phi\rangle = &\sum_{i,\sigma}\int \mathrm{d}r\, \psi_i^{\sigma*}(r)[-\frac{1}{2}\nabla^2 + V_{ext}(r)]\psi_i^{\sigma}(r) + E_{11} \\ &+\frac{1}{2}\sum_{i,j,\sigma_i\sigma_j}\int \mathrm{d}r\,\mathrm{d}r'\, \psi_i^{\sigma*}(r)\psi_j^{\sigma*}(r')\frac{1}{|r-r'|}\psi_i^{\sigma_i}(r)\psi_j^{\sigma_j}(r') \\ &-\frac{1}{2}\sum_{i,j,\sigma}\int \mathrm{d}r\,\mathrm{d}r'\, \psi_i^{\sigma*}(r)\psi_j^{\sigma*}(r')\frac{1}{|r-r'|}\psi_i^{\sigma}(r)\psi_j^{\sigma}(r') \end{aligned} \tag{4.5}$$

where the first term groups together the single expectation values summed over orbitals. The third term describe the direct interactions among electrons, while the exchange interaction is described by the fourth term. Notice that there is double summation in the third and fourth terms. Considering a situation where the spin functions are quantized along an axis, then the variation of $\psi_i^{\sigma*}(r)$ for each spin σ can be expressed as

$$\left[-\frac{1}{2}\nabla^2+\sum_{i,\sigma_j}\int \mathrm{d}r'\psi_i^{\sigma_j*}(r')\psi_j^{\sigma_j*}(r')\frac{1}{|r-r'|}\right]\psi_i^{\sigma}(r)$$
$$-\sum_j\int \mathrm{d}r'\psi_j^{\sigma*}(r')\psi_i^{\sigma}(r')\frac{1}{|r-r'|}\psi_j^{\sigma}(r)=E_i^{\sigma}\psi_i^{\sigma}(r) \tag{4.6}$$

which defines the Hartree-Fock equation. Modification of equation 4.6 gives a Schrödinger-like equation with an effective Hamiltonian operator that depends on the state

$$\hat{H}^i_{eff}\psi_i^{\sigma}(r)=\left[-\frac{\hbar^2}{2m_e}\bigtriangledown^2+\hat{V}^{i,\sigma}_{eff}(r)\right]\psi_i^{\sigma}(r)=E_i^{\sigma}\psi_i^{\sigma}(r) \tag{4.7}$$

The effective potential $\hat{V}^{i,\sigma}_{eff}(r)$ that acts on each electron of spin σ at point r is expressed as

$$\hat{V}^{i,\sigma}_{eff}(r)=V_{ext}(r)+V_{Hartree}(r)+\hat{V}^{i,\sigma}_{x}(r) \tag{4.8}$$

and the exchange term operator $\hat{V}_x$ is given by a sum over orbitals of the same spin σ

$$\hat{V}^{i,\sigma}_{x}(r)=-\sum_j\int dr'\psi_j^{\sigma*}(r')\psi_i^{\sigma}(r')\frac{1}{|r-r'|}\frac{\psi_j^{\sigma}(r)}{\psi_i^{\sigma}(r)} \tag{4.9}$$

note that $\sum_j\psi_j^{\sigma*}(r')\psi_i^{\sigma}(r')$ is the coulomb potential due to the exchange charge density for each state i,σ.

4.4 Density Functional Theory (DFT)

For about five decades density functional theory (DFT) has been widely used as a primary tool for the electronic structure properties calculations of solid systems.

The DFT was developed by Hohenberg, Kohn and Sham [53, 54] and it gives very accurate description of ground state properties of solids and molecules. DFT is based on the electronic density distribution $n(r)$ rather than the many electron wave function Ψ [60]. In DFT an accurate ground state is crucial for the determination of equilibrium volume, bulk modulus, lattice constants etc. DFT not only allows for the simulation of simple electronic properties, but also it allows for the treatment of quite complex material's properties. This involves the determination of magnetic and electric susceptibilities, spin polarized ground states, superconductivity etc [60]. Besides the determination of ground state properties using DFT, one may also describe the excited state properties to a certain extent. This is based on the fact that the ground-state density of an electronic system determines not only its electron number but also the external potential, which is associated with a specific Hamiltonian operator. This specific Hamiltonian operator fully describes the ground state as well as the excited states [61].

4.4.1 The Hohenberg-Kohn Theorem

The Hohenberg-Kohn Theorem [53] states that if N interacting electrons move in an external potential V_{ext}, there is a unique ground-state electron density $n_0(\mathbf{r})$ which minimizes the energy functional

$$E[n] = F[n] + \int n(\mathbf{r}) V_{ext}(\mathbf{r}) \mathrm{d}\mathbf{r} \tag{4.10}$$

where F is a universal functional of n. The resulting minimum value of the functional E is E_0, which is the ground-state electronic energy. A particular simple

proof of the Hohenberg-Kohn theorem may be given as follows [62]: Defining an N-electron functional F as

$$F\left[n(r)\right] = \min_{|\Psi \to n(r)|} \left\langle \Psi | \hat{F} | \Psi \right\rangle, \tag{4.11}$$

where the expectation value is determined by searching over all N-electron wave functions, Ψ, which reduce to density $n(\mathbf{r})$ one then selects the wave function Ψ which effectively minimizes the expectation value of F. Next specify F as

$$\hat{F} = \sum_i -\frac{1}{2} \bigtriangledown_i^2 + \frac{1}{2} \sum_{i \neq j} \frac{1}{|\mathbf{r_i} - \mathbf{r_j}|}. \tag{4.12}$$

Consider an N-electron ground state wave function Ψ_0 which yields density n_0. Then the ground state energy is

$$E_0 = \left\langle \Psi_0 | \hat{F} + \hat{V}_{ext} | \Psi_0 \right\rangle \tag{4.13}$$

From definition, equation (4.11),

$$F\left[n_0\right] = \min_{\Psi \to n_0} \left\langle \Psi | \hat{F} | \Psi \right\rangle = \left\langle \Psi^0_{min} | \hat{F} | \Psi^0_{min} \right\rangle, \tag{4.14}$$

and from the minimal principle

$$F\left[n_0\right] + \int n_0(r) d^3 r = \left\langle \Psi^0_{min} | \hat{F} + \hat{V}_{ext} | \Psi^0_{min} \right\rangle \geqslant E_0 \tag{4.15}$$

However, since

$$F[n_0] = \left\langle \Psi^0_{min} | \hat{F} | \Psi^0_{min} \right\rangle \leq \left\langle \Psi_0 | \hat{F} | \Psi_0 \right\rangle \tag{4.16}$$

we also have

$$F[n_0] + \int n_0(r) d^3r = \left\langle \Psi^0_{min} | \hat{F} + \hat{V}_{ext} | \Psi^0_{min} \right\rangle \leq E_0 \tag{4.17}$$

since Ψ^0_{min} and Ψ_0 yield the same density n_0. From equations (4.15) and (4.17) it follows that

$$E[n_0] = F[n_0] + \int n_0(r) d^3r = E_0 \tag{4.18}$$

thereby completing the proof.

4.4.2 The Kohn-Sham Equations

Description of properties of solids from *ab-inition* calculation involves solving the Kohn-Sham equations, which are a general set of one particle equations. The accurate and time efficient methods for solving these equations remains a big challenge. So far, various simplifying methods have been proposed but each of these methods has got its limitations. For example the *muffin-tin approximation* methods are based on the observation that the potential is atomic-like around the lattice sites and almost flat between the atoms of a solid [63, 64]. This method has its most prominent application in variational method developed by Korringa, Kohn and Rostocker [65–67]. Other approximation methods include pseudopotential methods which substitute the inert atomic cores by a model potential, and orthogonalize a set of pseudo-valence states to these model cores [68, 69].

Kohn and Sham [54] derived their general coupled set of differential equations to determine the ground-state density $n_0(\mathbf{r})$ of a non-interacting reference system. To this end Kohn and Sham separated $F[n(\mathbf{r})]$ into four distinct parts and the functional E becomes

$$E[n(\mathbf{r})] = T_s[n(\mathbf{r})] + \frac{1}{2}\int\int \frac{n(\mathbf{r})n(\mathbf{r}')}{|\mathbf{r}-\mathbf{r}'|}d\mathbf{r}d\mathbf{r}' + E_{XC}[n(\mathbf{r})] + \int n(\mathbf{r})V_{ext}(\mathbf{r})d\mathbf{r}, \quad (4.19)$$

where $T_s[n(\mathbf{r})]$ is defined as the kinetic energy of a non-interacting electron gas with density $n(\mathbf{r})$, i.e.

$$T_s[n(\mathbf{r})] = -\frac{1}{2}\sum_{i=1}^{N}\int \Psi_i^*(\mathbf{r})\nabla^2\Psi_i(\mathbf{r})d\mathbf{r}. \quad (4.20)$$

Equation (4.19) also defines the exchange-correlation functional $E_{XC}[n]$. Imposing a normalization constraint on the electron density, $\int n(\mathbf{r})d\mathbf{r} = N$, they obtained the following variational principle

$$\begin{aligned} \frac{\delta}{\delta n(\mathbf{r})}\left[E[n(\mathbf{r})] - \mu\int n(\mathbf{r})\mathbf{dr}\right] &= 0 \\ \Rightarrow \frac{\delta E[n(\mathbf{r})]}{\delta n(\mathbf{r})} &= \mu. \end{aligned} \quad (4.21)$$

Equation 4.21 may now be re-written in terms of an effective potential, $V_{eff}(\mathbf{r})$, and that

$$\frac{\delta T_s[n(\mathbf{r})]}{\delta n(\mathbf{r})} + V_{eff}(\mathbf{r}) = \mu, \quad (4.22)$$

where

$$V_{eff}(\mathbf{r}) = V_{ext}(\mathbf{r}) + \int \frac{\mathbf{n}(\mathbf{r})}{|\mathbf{r}-\mathbf{r}|}\mathrm{d}\mathbf{r}' + V_{XC}(\mathbf{r}) \quad (4.23)$$

with

$$V_{XC}(\mathbf{r}) = \frac{\delta E_{XC}[n(\mathbf{r})]}{\delta n(\mathbf{r})}, \tag{4.24}$$

It is important to note that non-interacting electrons moving in an external potential $V_{eff}(r)$ are described by a ground state density

$$n_0(\mathbf{r}) = \sum_{i=1}^{N} |\psi_i(\mathbf{r})|^2, \tag{4.25}$$

To determine the ground state energy E_0 one has to solve the following one electron Schrödinger equation

$$\left(\frac{1}{2}\nabla_i^2 + V_{eff}(r) - E_i\right)\psi_i(r) = 0 \tag{4.26}$$

and this set of equations should be solved self-consistently as

$$V_{eff}(r) = V_{eff}(n_0(r)). \tag{4.27}$$

The above equations (4.22) and (4.23) and the assumption of a non-interacting reference system provide a theoretically exact method for finding the ground state energy of an interacting system, provided that the form of E_{XC} is known. The application of DFT requires the use of various approximate forms for the E_{XC} such as the local density approximation [70] and the generalized gradient approximation [71].

4.5 The Local Density Approximation (LDA)

Within the framework of the local density approximation (LDA) [70, 72, 73], the value of $E_{XC}[n(\mathbf{r})]$ is approximated by the exchange-correlation energy of an electron in a homogeneous electron gas of density $n(\mathbf{r})$, i.e.,

$$E_{XC}^{LDA}[n(\mathbf{r})] = \int \mathbf{E}_{XC}(n(\mathbf{r}))n(\mathbf{r})d\mathbf{r}. \tag{4.28}$$

The LDA functional reproduces the ground state properties of many systems very accurately. For example, the bulk properties of group 4d and 5d transition metals are well described by LDA. However, there are situation whereby LDA fails. For example LDA predict the wrong magnetic structure of iron [74, 75]. LDA also predicts inaccurately the band gap of semiconductor materials [76–78].

4.6 Generalized gradient approximation (GGA)

For a long time the local density approximation was considered the method of choice in electronic structure calculations. One strategy to improve upon LDA is to include the gradient of the charge density in exchange-correlation functional, something that should take into account the inhomogeneity of the electron gas. The resulting method, where the XC potential is a function of both the charge density (at a given point), and the first-order gradient of the charge density (at the same point), is known as the generalized gradient approximation (GGA) [71, 79, 80].

$$E_{XC}^{GGA}[n] = \int d^3r f(n, \nabla n) \tag{4.29}$$

the $E_{XC}^{GGA}[n]$ is the exchange correlation energy per particle of an electron gas. The GGA method gives better total energies, especially for small molecules, but computationally it is more time consuming than LDA [81]. Generally, GGA has the following advantages over LDA [82, 83]:

1. GGA improves ground state properties for light atoms, molecules and clusters.

2. GGA predicts the correct magnetic properties of 3d transition metals such as body centered iron.

Though GGA seems to be superior compared to LDA, it has several drawbacks. The GGA methods fails to accurately treat the hydrogens bond. This defect is clearly manifested through expansion and hence softening of bonds [84].

4.7 Pseudopotentials

As mentioned in previous sections, practical solutions to the self-consistent Kohn-Sham equations are subject to various approximations. Methods have been developed to reduce the computational cost (rapid convergence) without compromising the outcome of the calculations. The first-principle pseudopotential methods [85–87] consider the valence electrons only, excluding the deep-inner core states and the strong potential that binds them to the nuclei. This makes the calculation less computationally expensive as compared to full-potential methods. Normally, the core electrons have minimal influence on the properties of solids, but their proper inclusion into the pseudopotentials creates room for the sufficient use of plane-

wave basis sets in electronic structure calculations [88–90]. There are several types of pseudopotentials: norm-conserving pseudo potentials [91, 92], ultra-soft pseudo potentials [93] and projector augmented wave (PAW) type of pseudopotentials [94]. The PAW method is a unique method for determination of the electronic structure of materials since it describes well the nodal behavior of the valence-electron wave function, and it also allows for the inclusion of the upper core states into the self-consistent iterations procedure [95, 96].

4.8 K-points

The Monkhorst-Pack grid is a common technique used in sampling the Brillouin zone. This method generates special points in the Brillouin zone, and their integration weights which provides an efficient means of integrating periodic functions in k-space [97]. The accuracy of integration entirely depends on the choice of integration grid, and therefore the Monkhorst-Pack technique allows for specific integration of portions of Brillouin zone only, but also for a sampling of the entire Brillouin zone. However, the symmetry of the cell may drastically reduce the number of k-points within the Brillouin zone.

Chapter 5

Computational Details

5.1 Introduction

Calculation in this work were done using density functional theory (DFT) [98, 99]. The projector augmented wave pseudo-potentials [100] were used all throughout to represent the valence electrons. The electron-electron interaction was treated within the local density approximation [101] using the Ceperley-Alder exchange correlation potential [72] as implemented in the Vienna *Ab initio* Simulation Package (VASP) [102–104]. An energy cutoff of 500 eV was found to be sufficient for providing a proper plane wave basis set. For Brillioun-zone integration the Monkhorst-Park [97] special *k*-point sampling method was the method chosen for both the superhard and precursor bulk phases. The *k*-point mesh of 8x8x8 for cubic-spinel and 12x12x12 *k*-point mesh for all structures are employed. For computations using the plane wave Quantum ESPRESSO code [105], ultrasoft Vanderbilt pseudopotentials [93] and a cutoff energy of 35 Rydberg were used. The optimized geometries of the

structures were found using unconstrained relaxation of atoms.

5.2 Vienna Ab-Initio Simulation Package (VASP)

The VASP code was developed by Kresse and Hafner [102–104]. It is a plane-wave DFT code which uses projector-augmented wave (PAW)[106] and ultra-soft Vanderbilt pseudo potentials(UP-PP)[93] to describe the electron core interactions. The PAW method has received considerable attention because of its reliability in accurately and sufficiently determining the electronic structure of materials. The PAW method preserves the Physics of all-electron calculation as well as the nodal behavior of the valence-electron wave functions. The uniqueness of PAW method stems from the way it splits the wave function in sections or parts [95].

The DFT approach implemented in VASP is based on the (finite-temperature) local-density approximation, with the free energy as variational quantity, and an exact self consistent evaluation of the instantaneous electronic ground state at each nuclear time step [107]. Salient features in VASP includes the symmetry code used to set up the Monkhorst Pack special points, which allows for an efficient calculation of bulk properties etc. VASP is capable of integrating the band-structure energy over the Brillouin zone by using various smearing or tetrahedron methods. These approaches are meant to moderate convergence with respect to the number of special points. Some other applications of VASP includes, structural optimization, molecular dynamics on the ground-state Born-Oppenheimer surface, Nudged Elastic Band (NEB) and Fourier String Method Dynamics [107].

5.3 Quantum ESPRESSO (QE)

Quantum ESPRESSO [105] stand for opEnSource Package for Research in Electronic Structure, Simulation, and Optimization. It is a free software, released under the GNU General Public License. The code is designed to perform density functional theory calculations of the electronic structure. It uses plane wave basis sets and pseudopotential in its applications. Its features range from the calculation of ground-state energy and Kohn-Sham orbitals to the calculation of atomic forces, stresses, and structural optimization, molecular dynamics on the ground-state Born-Oppenheimer surface, Nudged Elastic Band (NEB) and Fourier String Method Dynamics. Quantum ESPRESSO is also able to perform other calculations such as; phonon frequencies and eigenvectors at a generic wave vector, effective charges and dielectric tensors, electron-phonon interaction coefficients for metals, Infrared and Raman (nonresonant) cross section etc. [105].

The main advantages of QE over VASP in the context of this work are as follows: first, QE is able to characterize the vibrational frequencies into either Raman or infrared active modes. Secondly, QE assigns modes on the basis of the degeneracy of the vibrational frequencies (single, double or triple). In addition, QE tells you to which irreducible representation a mode belongs. This makes it easy to interpret the results of Raman and infrared spectra.

5.4 Equation of states

Several equations of states (EoS) have been proposed to describe the total energy or pressure as a function of volume and temperature. Some of them make rather specific assumption about the bulk modulus, pressure derivative of the bulk modulus, interatomic potentials, strain functions etc [108–111]. The Murnaghan equation of state is

$$P(V) = \frac{B_0}{B_0'}\left[\left(\frac{V_0}{V}\right)^{B_0'} - 1\right], \tag{5.1}$$

and the approach is preferred for low compression. The Vinet equation of state is

$$\begin{aligned} E(V) = &-\frac{4B_0V_0}{(B_0'-1)^2}\left(1-\frac{3}{2}(B_0'-1)\left(1-\left(\frac{V}{V_0}\right)^{1/3}\right)\right) \\ &\exp\left(\frac{3}{2}(B_0'-1)\left(1-\left(\frac{V}{V_0}\right)^{1/3}\right)\right) \end{aligned} \tag{5.2}$$

which is preferred for liquid [112–114].

The Birch equation of state [115] is defined based on a series expansion of pressure

$$P(f) = 3B_0 f(1+2f)^{\frac{5}{2}}[1+\frac{3}{2}(B_0'-4)f] \tag{5.3}$$

where f is the Eulerian strain expressed as

$$f = \frac{1}{2}\left[\left(\frac{V}{V_0}\right)^{-\frac{2}{3}} - 1\right] \tag{5.4}$$

V_0 is the equilibrium volume in the above expressions and the pressure, bulk modulus and the pressure derivative of the bulk modulus are given respectively by

$$P = -\frac{\partial E}{\partial V}. \tag{5.5}$$

$$B = -V\left(\frac{\partial P}{\partial V}\right)_T \tag{5.6}$$

and

$$B^{'} = \left(\frac{\partial B_0}{\partial P}\right)_T. \tag{5.7}$$

Equation (5.5) shows that the pressure is the negative (volume) derivative of the total energy E, the bulk modulus measures the curvature of the energy versus volume curve at a give volume V. In particular B_0 and B_0' indicate that B and B' are evaluated at an equilibrium volume V_0.

5.5 Phonon frequency

The first-principle calculations of vibrational frequencies for graphite and various phases of C_3N_4 have been performed using VASP and Quantum ESPRESSO. I started from numerically optimized structures of graphite, cubic C_3N_4, defect zinc-blende C_3N_4, spinel C_3N_4, hexagonal C_3N_4, rhombohedral and orthorhombic C_3N_4. Previous optimization of these structures is important, since well converged Brillouin zone grids and cut-off energies minimize numerical errors for vibrational modes. Figure 5.1 shows the first Brillouin zone of the two dimensional reciprocal lattice for graphite. The phonons within and on boundary correspond to standing waves. Vibrational modes mainly arise from high symmetry points [116, 117] for example those with k1=k2=k3=0 at Γ point.

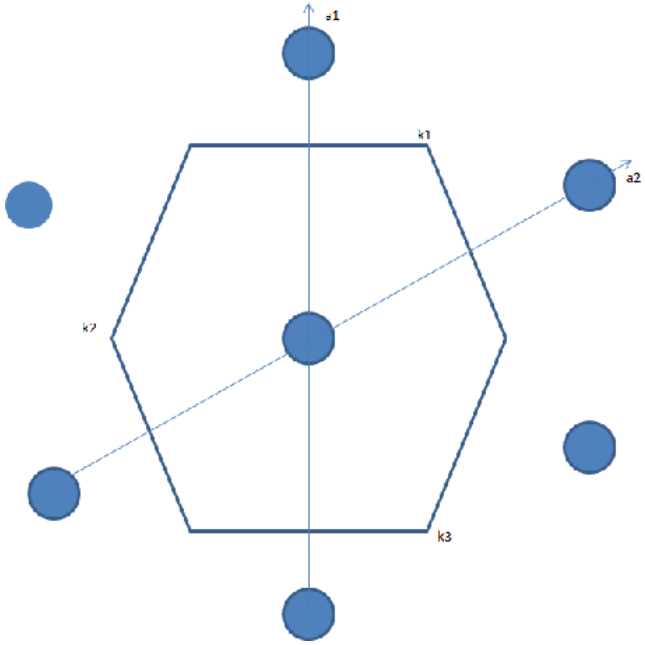


Figure 5.1 The first Brillouin zone of the two dimensional graphite reciprocal lattice. The gamma point (wave vector k=0) lies at the center of the Brillouin zone. k1=k2=k3 are high symmetry points, while a1 and a2 are reciprocal lattice vectors.

The vibrational spectra are obtained from the relative intensities of vibrations, which can be related to the eigenvectors of the dynamical matrix [11]. For instance, cubic C_3N_4 has 28 atoms within the unit cell. The atoms vibrate along the x, y and z directions. Therefore, the probability for the localization of each atom at a phonon of frequency ω is described by

$$L(\omega) = d_x^2 + d_y^2 + d_z^2 \tag{5.8}$$

The total probability of localization $L(\omega)$ of the 28 atoms is obtained by summing up displacements along d_x, d_y and d_z in the x, y and z directions.

Chapter 6

Results and Discussion

6.1 Ground state properties

Liu and Cohen [5] suggested that β-C_3N_4 could be harder than diamond, based on the high bulk modulus they obtained on the basis of empirical methods. But up to date, diamond remains the hardest material ever known. This is due to diamond having the highest known shear modulus [118]. It is in this regard that I have investigated the shear and bulk modulus of six phases of C_3N_4, and compared the results to those of diamond. By definition, the shear modulus G is the resistance of a material to reversible deformation changing the shape of a sample, while the equilibrium bulk modulus B_0 is a measure of resistance towards the change of volume of a material subject to an applied external pressure [2].

Table 6.1 The space groups of eight crystals structures and calculated first principles total energy in (eV), bulk modulus in (GPa), derivative of bulk modulus and equilibrium volume in ($Å^3$) obtained using Birch equation of state.

Z	Space group	E_0	B_0(this work)	B_0 (others)	$B_0^{'}$(this work)	$B_0^{'}$(others)	V_0(this work)	V_0 (others)
Diamond	F_{d-3m}	-9.09	432.82	459[h]	3.69		38.52	
Graphite	P_{63mc}	-9.20	245.57		3.56		66.84	
ZB	P_{-43m}	-9.10	434.3	430[a], 425[d]	3.80	3.40[d]	37.73	
Cubic	I_{-43d}	-9.13	477.9	480[a], 496[e]	3.81	3.30[a]	37.69	
Spinel	F_{d-3m}	-8.12	433.6	369[b], 415[f]	4.18	3.85[b]	36.07	37.41[g]
g-C_3N_4	P_{6m2}	-9.28	221.8	253[c]	4.35		56.92	
g-C_3N_4	R_{3m}	-9.28	222.7	51[d]	4.28		56.96	
g-C_3N_4	P_{25}	-9.25	156.99		4.13		73.89	

[a]Reference [119],
[b]Reference [120],
[c]Reference [21],
[d]Reference [25],
[e]Reference [20],
[f]Reference [121]
[g]Reference [122],
[h]Reference [123]

I have calculated the bulk modulus using two different approaches. In the first approach, I determine the bulk modulus and its pressure derivative using the pseudopotential method to compute the energy versus volume at series of data points. Then I fitted those values to the Birch equation of state [124]. The calculated values of equilibrium energy E_0, bulk modulus B_0, derivative of the bulk modulus $B_0^{'}$ and equilibrium volume V_0 are summarized in Table 6.1. The graphitic phases are the most energetically-favorable structures, as suggested by the lowest ground state energies. Note that based on the bulk modulus, cubic C_3N_4 is harder than diamond. This suggests that C_3N_4, if synthesized, could be a perfect substitute for diamond in various industrial applications. The bulk modulus of cubic C_3N_4, spinel and zinc-blende C_3N_4 structures agree well with other theoretical values reported before [125, 126]. The calculated bulk modulus of diamond is in good agreement with experimental value reported elsewhere [127]. The graphitic structures are soft with bulk moduli, almost half the one of super-hard phases.

6.2 Elastic constants

In this section we present the results of independent elastic constants for diamond, graphite and carbon nitride as well as other elastic constants derived from them. Diamond and graphite are benchmark cases, because their elastic constants are well known from theoretical and experimental studies. Starting from the optimized structures, we extracted the elastic constants by applying a uniform deformation to the unit cell and calculated the yield stress [128], as implemented in VASP.

Table 6.2 Calculated zero pressure elastic constants C_{ij} (GPa) for various C_3N_4 phases, diamond and graphite.

Space group	Diamond F_{d-3m}	Graphite P_{63mc}	ZB P_{-43m}	Cubic I_{-43d}	Spinel F_{d-3m}	g-C_3N_4 P_{6m2}	g-C_3N_4 R_{3M}	g-C_3N_4 P_{25}
Z	8	4	7	28	56	14	21	7
c_{11}(this work)	1097	1054	865	861	536	794	862	5.1
c_{11}(others)	1060[c]		840[a]	863[b]			870[a]	
c_{12}(this work)	150	192	221	300	395	174	174	-2.7
c_{12}(others)	125[c]		213[a]	313[b]			148[a]	
c_{44}(this work)	595	5.0	467	469	539	3.7	8.9	-0.4
c_{44}(others)	562[c]		452[a]	348[b]			14[a]	
c_{13}(this work)	150	-2.92	221	300	395.4	-3.4	-1.6	-2.3
c_{13}(others)			213[a]				-3[a]	
c_{14}(this work)	0	0	0	0	0	-0.3	0	0
c_{14}(others)			0[a]				1[a]	
c_{33}(this work)	1097	42	865	861	536	13	57	624
c_{33}(others)			840[a]				57[a]	
c_{22}(this work)	1097	1054	865	861	536	793	862	619
c_{23}(this work)	150	-2.7	221	300	395	-6.5	-1.6	95
c_{55}(this work)	595	5	467	469	539	-8.5	8.9	206
c_{66}(this work)	595	431	467	469	539	308	344	-0.7

[a]Reference [25], [b]Reference [20], [c]Reference [127]

Cubic crystal structures have three independent elastic constants C_{11}, C_{12}, and C_{44}. The hexagonal structures have five independent elastic constants (C_{11}, C_{12}, C_{13}, C_{33} and C_{44}). The rhombohedral and orthorhombic crystal structures have six (C_{11}, C_{12}, C_{13}, C_{14}, C_{33}, and C_{44}) and nine (C_{11}, C_{12}, C_{13}, C_{22} ,C_{23}, C_{33}, C_{44}, C_{55} and C_{66}) independent elastic constants respectively. The calculated values of elastic constants are presented in Table 6.2. The independent elastic constants for cubic-C_3N_4 are similar to those obtained by Teter *et al* [20]. These authors determined the elastic constants using norm-conserving Troullier Martins pseudopotentials. The slight difference in C_{44} can be attributed to the use of a different pseudopotential. The elastic constants for defect in zinc-blende are also in good agreement with other theoretical studies [25]. The mechanical stability test [129] is satisfied for all independent elastic constant in cubic systems, as C_{11}, C_{22} and C_{44} are all positive. On the other hand, the negative values of some elastic constants of g-C_3N_4 indicate mechanical instability for these structures.

6.3 Elastic moduli

The elastic bulk modulus B, shear modulus G, Young's modulus and Poisson's ratio ν based on the Voigt-Reuss-Hill approximations [130, 131] are presented in Table 6.3. Within the Voigt approximation, the general expression of bulk and shear moduli are

$$B_V = \left[(C_{11}+C_{22}+C_{33})+2(C_{12}+C_{13}+C_{23})\right]/9 \tag{6.1}$$

and

$$G_V = [(C_{11}+C_{22}+C_{33})-(C_{12}+C_{13}+C_{23})+3(C_{44}+C_{55}+C_{66})]/15 \quad (6.2)$$

and within the Reuss approximation

$$B_R = 1/[(S_{11}+S_{22}+S_{33})+2(S_{12}+S_{13}+S_{23})] \quad (6.3)$$

and

$$G_R = 15/[4(S_{11}+S_{22}+S_{33})-4(S_{12}+S_{13}+S_{23})+3(S_{44}+S_{55}+S_{66})]. \quad (6.4)$$

For cubic systems it follows that C_{11}=C_{22}=C_{33}, C_{12}=C_{13}=C_{23}, C_{44}=C_{55}=C_{66} and S_{11}=S_{22}=S_{33}, S_{12}=S_{13}=S_{23} and S_{44}=S_{55}=S_{66}. Applying these conditions to equations 6.1, 6.2, 6.3 and 6.4 one obtain

$$B_V = [C_{11}+2C_{12}]/3, \quad (6.5)$$

$$G_V = [C_{11}-2C_{12}+3C_{44}]/5 \quad (6.6)$$

and

$$B_R = 1/[3(S_{11}+2S_{12})], \quad (6.7)$$

$$G_R = 5/[4(S_{11}-4S_{12}+3S_{44})]. \quad (6.8)$$

Relating the cubic elastic compliance to the cubic elastic constants yields

$$S_{11} + 2S_{12} = 1/\left[C_{11} + 2C_{12}\right], \tag{6.9}$$

$$S_{11} - S_{12} = 1/\left[C_{11} - C_{12}\right] \tag{6.10}$$

and

$$S_{44} = \frac{1}{C_{44}}. \tag{6.11}$$

This indicates that for a cubic crystal B_V=B_R. The average bulk modulus B_H and shear modulus G_H are referred to as Hill bulk modulus and Hill shear modulus respectively. The B_H and G_H are expressed in Voigt and Reuss approximation as

$$B = (B_V + B_R)/2, \tag{6.12}$$

$$G = (1/2)(G_V + G_R)/2, \tag{6.13}$$

where B_V and B_R are Voigt and Reuss bulk modulus, respectively, and G_V and G_R are Voigt and Reuss shear moduli respectively. For rhombohedral structures, the shear and bulk moduli have been obtained using the following equations from reference [132]

$$B_V = (1/9)(2C_{11} + C_{33}) + (2/9)(C_{12} + 2C_{13}) \tag{6.14}$$

$$G_V = (1/15)(2C_{11} + C_{33} - C_{12} - 2C_{13}) + (1/5)(2C_{44} + ((C_{11} - C_{12})/2)) \tag{6.15}$$

$$B_R = 1/((2S_{11} + S_{33}) + 2(S_{12} + 2S_{13})) \tag{6.16}$$

$$G_R = 15/[4(2S_{11} + S_{33} - S_{12} - 2S_{13}) + 6(S_{44} + S_{11} - S_{12})] \tag{6.17}$$

where S_{ij} are components of the elastic compliance matrix. The S_{ij} are obtained in terms of the C_{ij} by inverting the elastic tensors.

The alternative method for obtaining bulk modulus B [133] of a rhombohedral structure in terms of C_{ij} is

$$B = [C_{33}(C_{11} + C_{12}) - 2C_{13}^2]/[C_{11} + C_{12} - 4C_{13} + 2C_{33}]. \tag{6.18}$$

Different approaches for the calculation of bulk and shear moduli, as shown in Table (6.1) (obtained by Birch equation of state) and Table (6.3) (obtained by Voigt-Reuss approach) turn out to lead to rather similar results. In all cases, cubic C_3N_4 is the hardest phase as indicated by its bulk modulus. Its shear modulus is 393 GPa, which is smaller than that of diamond.

Since the Voigt approximations yields the upper bound for the bulk and shear moduli, the lower bound is presented as Reuss values. The average of Voigt and Reuss values is equivalent to Hill's values, as shown in Table (6.3). For cubic systems, B_V=B_R and G_V=G_R, while for non cubic systems, Voigt and Reuss values are different.

The calculated ground state Young's modulus (Y) are listed in Table (6.3). Y is the ratio of stress against strain. It is a measures for the stiffness of a material. Y is expressed in the form of bulk and shear moduli

$$Y = [9B_H G_H]/[3B_H + G_H] \tag{6.19}$$

The magnitude of Y in cubic (935 GPa) and defect in zinc-blende (930 GPa) are similar. These values are less than that of diamond by as much as 200 GPa. Since Y is a measure of stiffness, a material with large Y is supposed to be stiff. In these present case, cubic and defect in zinc-blende C_3N_4 are stiffer than spinel structures, whose Y=834.80GPa. On the other hand, diamond with Y=1178 GPa, is the stiffest of all crystal structures considered in this work. Graphite with Y=521 GPa and graphitic structures whose Young's modulus ranges from 280-380 GPa are considerably less stiff.

When a beam of a certain material is stretched at both ends then there will be an increase in length along the longitudinal dimension. At the same time, there will be a decrease along the lateral dimension. The ratio of the decrease in lateral dimension(s) to the increase in longitudinal describes what is known as Poisson's ratio. The Poisson's ratio can be represented in terms of shear and bulk modulus as

$$\nu = [3B_H - 2G_H]/[2(3B_H + G_H)] \tag{6.20}$$

Using Poisson's ratio, ductility and brittleness of materials may be tested as suggested in reference [134]. For brittle material, ν is below 0.33, while for a ductile material, ν=0.33. Ductility is also estimated by applying Pugh's criteria [135]. According to Pugh, a material is ductile if $\frac{G_H}{B_H}$ is less than 0.5, otherwise the material is

brittle. The results here shows that all phases of C_3N_4 considered in this study are brittle, since they all have Poisson's ratio which are well below 0.33. Furthermore C_3N_4 also satisfies the Pugh's criteria for a brittle material.

Table 6.3 First principles elastic bulk modulus, shear modulus Young's modulus (all in GPa) and Poisson's ratio are presented.

	Diamond	Graphite	ZB	Cubic	Spinel	g-C3N4	g-C3N4	g-C3N4
	F_{d-3m}		P_{-43m}	I_{-43d}	F_{d-3m}	P_{6m2}	R_{3M}	P_{25}
Atom/cell	8	4	7	28	56	14	7	7
B_V	466	280	436	487	442	214	210	158
G_V	546	219	409	393	352	156	163	118
Y	1178	521	935	930	834	377	386	284
ν	0.08	0.19	0.14	0.18	0.19	0.21	0.19	0.20
B_R	466	38	436	487	442	12	45	4.89
G_R	539	11	395	369	147	19	20	-1.28
Hill B	466	159	436	487	442	113	127	81
Hill G	543	115	402	381	249	88	91	58

6.4 Covalent Bonds

The covalent bonding forms the strongest bonds compared to ionic, metallic and Van der Waals bonding. Generally, bonding in compounds affects the size and the shape of the structure. This is caused by a subtle interplay between the repulsion of the nuclei of bonded atoms and the attraction of the outer electrons of bonded atoms by the nuclei. Therefore, in covalently bonded atoms one can estimate the interatomic distances between those atoms by simply summing up the equivalent covalent radii [136]. In carbon nitride, there are three forms of covalent bonds, as presented in Table 6.4. As expected, the inter-atomic C-N distance is the shortest. From this work, I find that the graphitic carbon nitrides have shorter carbon-nitrogen bonds, compared to their cubic counter parts. A similar observation was made by Lowther[11]. It is observed that the inter atomic distances are directly proportional to the bulk modulus in graphic crystals and inversely proportional in cubic systems. Thus, in graphitic structures (orthorhombic, hexagonal and rhombohedral), the bulk moduli increase as the C-N bond length increase, while the bulk moduli in cubic structures (spinel, zinc blende and cubic) increases as the C-N bond lengths decreases. A reverse trend is observed with regard to C-C bond length in relation to bulk modulus. The C-C bond length of 1.55 Å in diamond is the shortest. Overall, the N-N bonding is longer than the the C-N bonding. This may be attributed to Coulumb repulsions among the nitrogen atoms.

Table 6.4 Equilibrium lattice parameters (a, b and c), bond lengths and bond angles of diamond and six phases of C_3N_4 at ground state. Lattice parameters and bond length are in Å, while bond angles are given in degrees.

	Diamond F_{d-3m}	Graphite	ZB P_{-43m}	Cubic I_{-43d}	Spinel F_{d-3m}	g-C_3N_4 P_{6m2}	g-C_3N_4 R_{3M}	g-C_3N_4 P_{25}
C-C	1.55	1.43	2.41	2.52	2.36	2.23	2.20	2.28
C-N			1.46	1.45	1.51	1.31	1.29	1.30
N-N			2.37	2.33	2.26	2.32	2.28	2.29
a	3.57, 3.54[b]	2.47	3.41,3.43[d]	5.38,5.39[c]	6.68,6.69[a]	4.73,4.74[c]	4.7	3.91
b	3.57, 3.54[b]	2.47	3.41	5.38	6.68,6.69[a]	4.09	4.7	4.74
c	3.57, 3.54[b]	6.73	3.41	5.38,5.39[c]	6.68,6.69[a]	6.14, 6.72[c]	9.1	4.12
α	90.00	90.00	90.00	90.00	90.00	90.00	90	90.00
β	90.00	90.00	90.00	90.00	90.00	90.00	90	90.00
γ	90.00	120.00	90.00	90.00	90.00	119.99	119.90	90.00

[a]Ref.[122], [b]Ref.[123], [c]Ref.[20], [d]Ref.[25].

Comparison of lattice constants (a, b and c) and bond angles (α, β and γ) with previous calculations of the cubic and graphitic phases of C_3N_4 is made. To start with, lattice constants (a=3.41 Å) for defect in zinc-blende are close to values of lattice constants (a=3.375 Å) reported in reference [35], (a=3.43 Å) in reference [25] and (a=3.423 Å) in reference [20].

Finally, the calculated lattice constants (a=3.57 Å) of diamond are in agreement with other theoretical values [123] as well as experimental values (a=3.567 Å), as reported in reference [137].

6.5 Effect of Hydrostatic Pressure

Pressure is a parameter that has a great effect on the properties of a material. As is well known, pressure changes the lattice parameters without necessarily changing the basic atomic network. In searching for new super-hard material, the effect of pressure need to be understood, so that optimum choices could be made based on the behavior of the material. Using first principles calculations, the effect of hydrostatic pressure on structural and electronic properties of defect zinc-blende phase is discussed. The task is to determine whether the bond length expand or decrease when a material is under pressure. In addition, the effect of hydrostatic pressure on the bulk moduli and elastic constants is examined. This is achieved by calculating total energies at different pressures and determine the minimum corresponding to optimized internal structural parameters.

Figure 6.1 shows the volume ratio (V/V_0) as a function of pressure for the defective zinc blende C_3N_4 polymorph. The ratio V/V_0 decreases as pressure increases. This happens because the atoms become in closer contact and have stronger interactions since the valence electron densities increase. Further compression may be resisted and within this pressure range the material will have (in principle) a constant bulk modulus [138].

6.6 Effect of pressure on elastic constants

In determining the elastic constants in a certain range of pressures, the symmetry of a cubic crystal under hydrostatic compression is preserved. Thus the relation

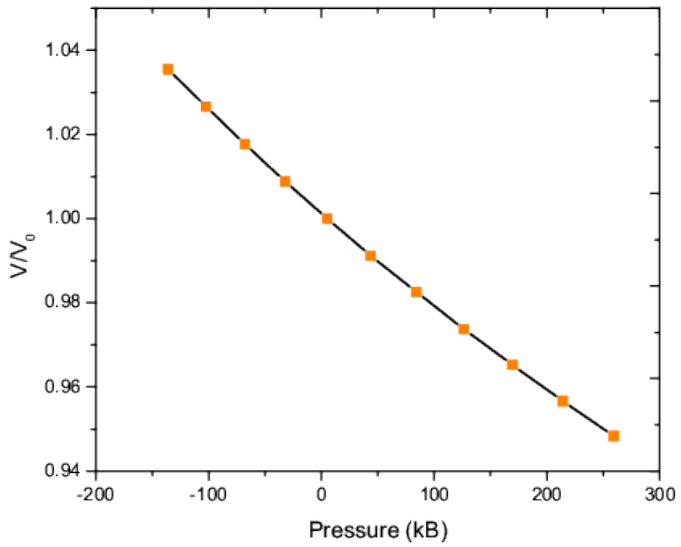


Figure 6.1 Volume - pressure relationship of defective zinc-blende-C_3N_4.

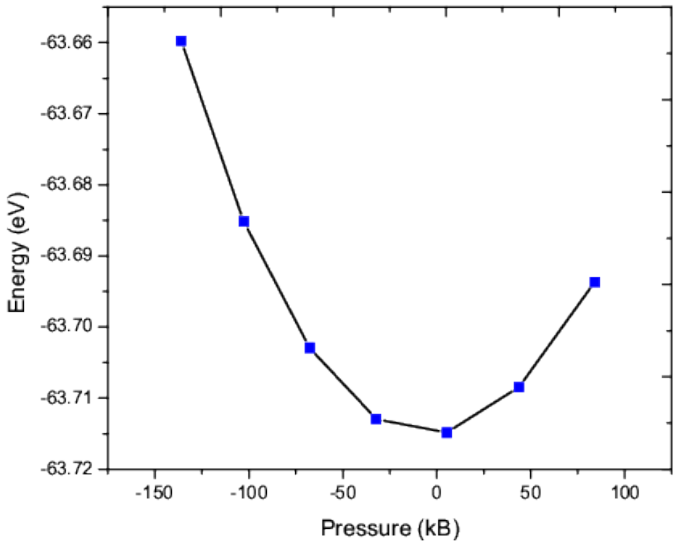


Figure 6.2 Total energy - pressure relationship in defective zinc-blende-C_3N_4.

between additional stresses and the infinitesimal strains must have the same form as for a cubic crystal under infinitesimal strain at zero pressure [46]. Therefore, was long as this condition is fulfilled, the effective elastic constants will entirely depend

on the induced pressure .

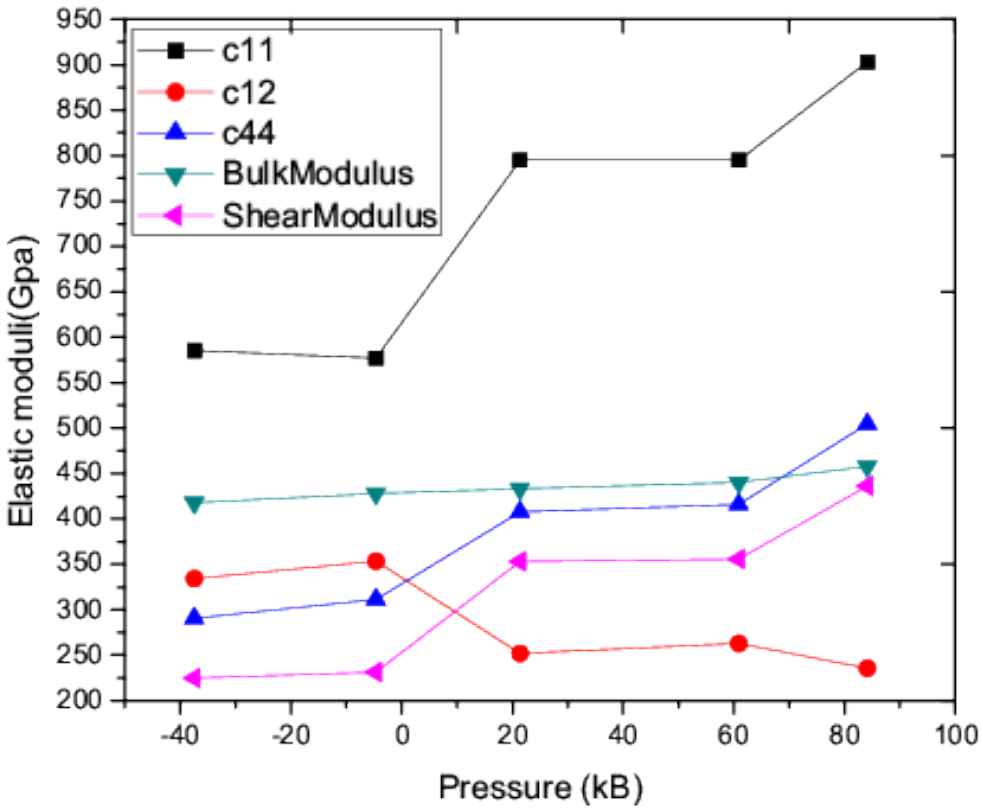


Figure 6.3 Bulk modulus, shear modulus and the three independent elastic constants; C_{11}, C_{12}, C_{44} as of C_3N_4 in defective zinc-blende structure.

It is a general observation that the elastic constants of a stable structure increases with increasing of pressure [139]. Figure 6.3 shows that C_{11} and C_{44} elastic constants of C_3N_4 in defect zinc-blende structure increase as the pressure increase. However, C_{12} decreases as hydrostatic pressure increase. This is an indication of an elastic instability of this structure at high pressure.

6.7 Vibrational Frequencies

The vibrational frequencies can be described in two ways: Firstly, if the dipole moment changes during vibration, light is emitted or absorbed. The frequency of vibration corresponds to light within the infrared region. Therefore a vibrational frequency absorbed within the infrared region is termed infrared active. Secondly, the vibrational frequency can be described in terms of the visible light scattering. The visible light may be absorbed and re-emitted under Rayleigh scattering. However, re-emission frequency may be reduced by the frequency of vibration resulting into a Raman scattering of light.

From group theoretical point of view, vibrations are infrared active if they belong to the same symmetry group as the component of dipole moment while, vibrations will be Raman active, if it belong to the same symmetry group as the components of the polarisability tensor.

Raman scattering and infrared reflectivity are popular methods among experimentalist for measuring the lattice dynamics of crystals [140, 141]. Vibrating atoms or molecules in a crystal involve periodic change of interatomic distance from their equilibrium positions. For harmonic vibrations, the displacement from the equilibrium position should be small enough so that the restoring force (F) is proportional to the displacement (x) as described by Hooke's laws (F=-kx) where k is a proportionality constant. Then the frequency of vibration is $\upsilon=\frac{1}{2\pi}\sqrt{\frac{k}{\mu}}$, where μ is the reduced mass of the system of atoms in consideration [142].

Symmetry of crystal structures plays a pivotal role in determining vibrational spectra of materials. The symmetry provides some information whether the energy

(or frequency) is zero or nonzero. The symmetry also decides if the spectroscopic transition has finite probability or zero probability. It is worth noting that the symmetry alone does not tell us the exact value of the transition probability.As an example take N atoms in the primitive unit cell. Each atom has three degrees of freedom, which correspond to the three Cartesian coordinates (x, y and z). Then there are 3N degrees of freedom in total. This implies that 3N vibrational modes exists of which three are acoustic modes which occur as a result of positive and negative charge moving in the same direction. These acoustic modes will have frequencies equal to zero at the Γ-point. Some authors [143] regard the acoustic modes as translational degrees of freedom, and hence subtract them from the 3N modes. Each of the remaining modes is related to a particular symmetry operation. All of these symmetry operations form a space group, and for vibrations around Γ point, the space groups reduce to point groups. The symmetry elements of a point group can be classified as pure rotations C_n (where 360/n indicates the angle through which the rotation takes place), or inversion i, or a rotation-reflection S_n, which combines a rotation C_n followed by a reflection in the same symmetry plane σ_h perpendicular to axis C_n. Other symmetry operations include pure reflection σ and the identity E.

Attempts to synthesis crystalline C_3N_4 has been unsuccessful. The experimental work has always ended up with amorphous carbon nitride, which of course has its own technological usefulness such as protective coating on hard disks. In order to understand the underlying situation there has been an attempts interpret the Raman and infrared spectra of amorphous carbon nitride, with particular focus on the peaks occurring at 1350 cm^{-1} and 1550 cm^{-1} in infrared spectrum [144]. It is clear that

under some circumstances the infrared and Raman modes may be identical [145], but in normal circumstances a vibration will be infrared active if it belongs to the same symmetry group as the component of dipole moment while, a vibration will be Raman active, if it belongs to the same symmetry group as the components of the polarisability tensor. As for the case of amorphous carbon nitride, there has been a debate about the appearance of D and G peaks in the infrared as well as in the Raman spectrum. Kaufman *et al* [146] argue that it is due to incorporation of nitrogen in carbon nitride that breaks the symmetry of the sp^2 domains and on the other hand, Ferrari [144] argues that nitrogen does not activate the D and G Raman modes in infrared spectra and if this occurs, then it should be purely accidental. In this work the above argument does not arise since focus is on crystalline carbon nitride. The vibrational spectra of super-hard phases (defective zinc blende, cubic and spinel phases of C_3N_4) and graphitic phases are analyzed in full detail. Graphitic structures are of particular interest since they are known to be the precursors for super-hard phases of C_3N_4, as mentioned earlier in this work. Raman and infrared spectra in graphite-like structures mainly depend on the ordering of sp^2 sites, while in diamond-like structure, they mainly depend on the sp^3 sites.

The defect zinc blende, has a diamond-like structure, and its corresponding vibrational spectrum is shown in figure 6.4. The equation 5.8 is used to describe relative amplitude (relative intensities) of the vibration modes together with the normalized coordinates of the carbon and nitrogen atoms. The contributions from carbon and nitrogen to the amplitude of the each vibrational frequency is clearly shown in the figure 6.4. The purely nitrogen related vibrations are about 830 cm^{-1}

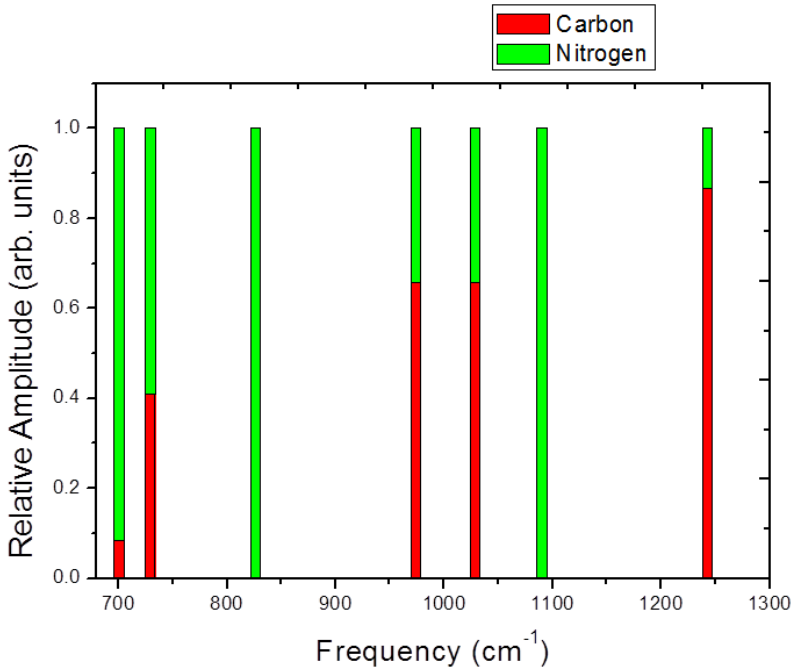


Figure 6.4 Calculated vibrational spectra of defect zinc-blende C_3N_4. The contributions of carbon and nitrogen atoms to the relative amplitudes of each vibrational frequencies are labeled in colour.

and 1100 cm^{-1}, while strong carbon related vibrations are about 1000 cm^{-1} and 1250 cm^{-1}. Table 6.5 contains a summary of vibrational frequencies of defective zinc-blende C_3N_4 obtained from VASP and Quantum ESPRESSO [105]. There are good agreement between these work and what had been done earlier by Rignanese *et al* [23].

The zinc-blende structure belongs to point group T_d(-43) and consists of five irreducible representation. The A_1 modes are nondegenerate while E modes and T modes are doubly and triply degenerate.

The point group T_d(-43) has in total twenty four symmetry operations. These symmetry operations are distributed as follows; one identity (E) symmetry operation, two fold rotation symmetry through an angle of 180 degrees at points (001, 010

Table 6.5 Calculated phonon frequencies of defective zinc-blende C_3N_4 with symmetry assignments (using VASP and Quantum ESPRESSO (QE)). The frequencies are given in cm^{-1}.

	This work QE	This work VASP	Others[23]
Raman			
A_1	961.6	976.7	990.5
E	1075.4	1094.2	1103
Infrared			
T_2	715.9	727.2	738.3
	982.8	1033.5	752.8
	1215.3	1246.1	1036.4
			1159.8
			1254.5
			1308.0
Silent			
T_2	727.4	729.9	741.8
	797.3	832.4	828.9

Table 6.6 Characters of the irreducible representations of point group T_d of C_3N_4 in a defect zinc-blende, cubic and spinel type of structures. The T_d group consist of the identity E, four threefold rotation axes C_3 (eight elements), three twofold axes C_2 (three elements), six reflection plane S_d(six elements) and three fourfold rotation-reflection axes (six elements). Each row in this table is an irreducible representation of the group.

	E	$8C_3$	$3C_2$	$6S_4$	$6\sigma_d$
A_1	1	1	1	1	1
A_2	1	1	1	-1	-1
E	2	-1	2	0	0
T_1	3	0	-1	1	-1
T_2	3	0	-1	-1	1

and 100), rotation through 120 degrees at Cartesian axes (-1-1-1, -111, 11-1, 1-11, 111, -11-1, 1-1-1 and -1-11), inversion and rotation through 180 degrees at Cartesian coordinates (110, 1-10, 101, -101, 011 and 01-1), an inversion and rotation through an angle of 90^o at points (00-1, 001, 0-10, 010, -100 and 100).

The cubic C_3N_4 structure also belong to point group T_d(-43) just like the defective zinc-blende structure. Figure 6.5 show the contributions of carbon and nitrogen atoms to each vibrational frequencies. The strong carbon related peak occur at

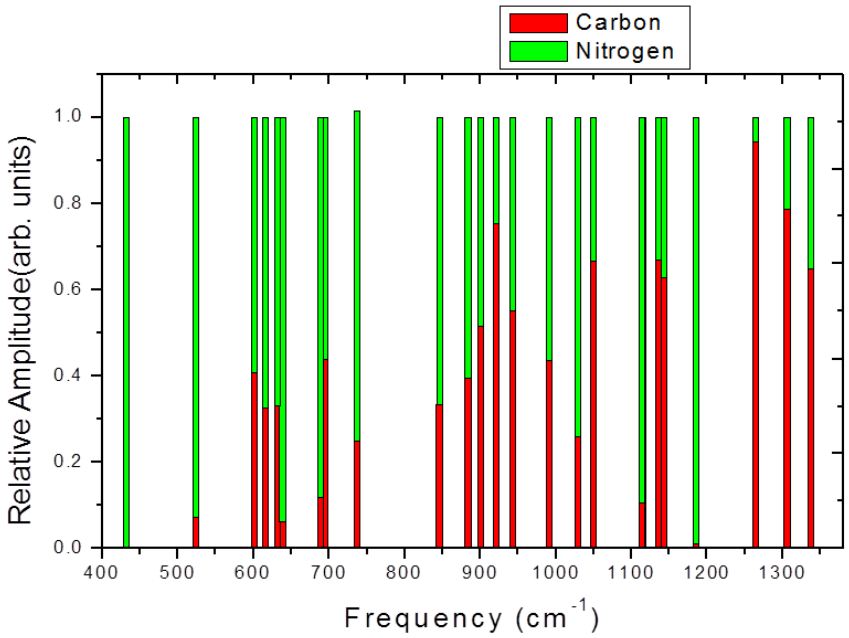


Figure 6.5 Vibrational spectra of cubic phase of C_3N_4. The contributions of carbon and nitrogen atoms to the relative amplitudes of each vibrational frequencies are labeled in colour.

about 1263 cm^{-1}. The nitrogen associated vibrational frequencies occur at lower energies of about 431 cm^{-1} and high energies of about 1184 cm^{-1}. The rest of frequencies have almost equal contributions from both carbon and nitrogen atoms. The summary of the vibrational frequencies of cubic C_3N_4 are presented in Table 6.7. These results agree well with frequencies observed by Rignanese *et al* [23]. The three degenerate modes (T) can be split into two parts i.e. T_1 and T_2 modes which are usually infrared active and inactive respectively. However, for the case of cubic C_3N_4, only the broad range of T modes are presented and not the divisions; T_1 and T_2.

The vibrational spectra of cubic spinel phase of C_3N_4 is shown in figure 6.6.

Table 6.7 Calculated phonon frequencies of cubic C_3N_4 with symmetry assignments. The frequencies are given in cm^{-1}.

	This work	Others[23]
Raman Active		
A	431	447
E	693	699.5
E	943	941.5
E	1184	1193.2
Infrared Active		
T	524	531.1
T	-	581.1
T	601	-
T		918.5
T		1059.4
T		1250.6
T	1142	-
T	1305	-
T	1333	-
Silent		
A	845	852
A	1049	1060.8
E	1115	-
T	689	680.8
T	-	820.3
T	-	956.8
T	-	1091.4
T	-	1131.9
T	883	-
T	920	-
T	990	-
T	1113	-
T	1263	-

The vibrational frequencies above 1200 cm^{-1} are predominantly associated with carbon atom. The strongest carbon related peak is about 1800 cm^{-1}. On the other hand vibrational frequencies below 1200 cm^{-1} are predominantly associated with nitrogen atom, with strongest nitrogen related peaks at about 550 cm^{-1} and 1109 cm^{-1}.

Table 6.8 show a range of both Raman and infrared vibrational frequencies. The

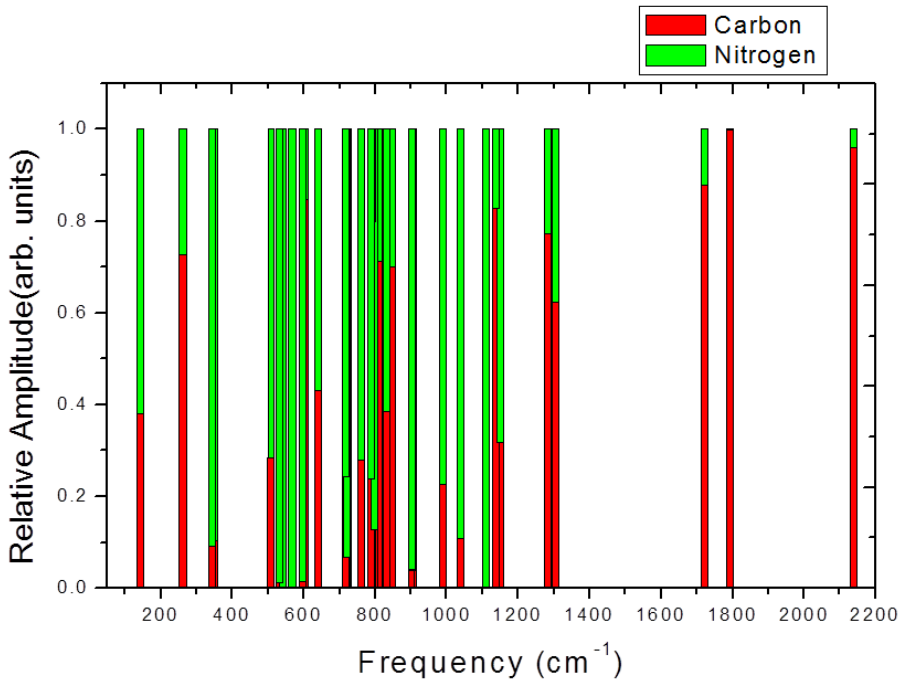


Figure 6.6 Calculated vibrational frequencies of cubic-spinel phase of C_3N_4. The contributions of carbon and nitrogen atoms to the relative amplitudes of each vibrational frequencies are labeled in colour.

available theoretical results [122] suggest infrared active modes at 239 cm^{-1}, 631 cm^{-1}, 752.8 cm^{-1} and at 1118 cm^{-1}. They also postulate Raman active modes at 351.6 cm^{-1}, 572 cm^{-1}, 801.8 cm^{-1}, 1044.6 cm^{-1} and 1113 cm^{-1}, which are in good agreement with results predicted in this work.

Generally, the spinel cubic system has A, E and T modes. Some of these modes are infrared active or Raman active as discussed above. The non-active modes are known as silent modes. Besides real modes in A, E and T, the VASP code calculates the imaginary modes (i). These imaginary modes could be Raman active or infrared active. They can also be silent modes. Imaginary modes are denoted by superscript i, e.g. 462^i, 795^i etc. Presence of imaginary modes indicates the instability of the

structure at zero pressure.

Table 6.8 Calculated phonon frequencies of cubic spinel C_3N_4, with tentative symmetry assignments. The frequencies are given in cm^{-1} and imaginary modes are presented as i.

	This work	Others[122]
Raman Active		
A	1109	1113.2
E	567	572
T	348	351.6
T	798	801.8
T	1037	1044.6
Infrared Active		
T	-	239.1
T	-	631.4
T	723	752.8
T	808	
T		1118.6
Silent		
A	905	883.9
A	1282	1282.8
A	2138	
E		216.3^i
E	462^i	
E	988	998.4
E	1148	
T	-	465.5^i
T	-	690
T	1792 1722	-
T	1303 901	-
T	848 832	-
T	716 639	-
T	604 598	-
T	531 508	-
T	342 261	-
T	141 155^i	-
T	726^i 749^i	-
T	795^i	-

In summary, the vibrational spectra of three super-hard phases are clearly distinguishable and hence it should be easy to identify various phases by observing the Raman vibrational spectra or the infrared vibrational spectra.

The graphitic C_3N_4 phases have similar characteristics like graphite as its dis-

cussed below. These graphitic structures comprise the hexagonal, rhombohedral and orthorhombic phases of C_3N_4. The summary of the vibrational frequencies for

Table 6.9 The full character table of the irreducible representations of point group C_{3h} for graphitic C_3N_4 in hexagonal structure. Each row in this table is an irreducible representation of the group.

	E	$C_3(z)$	$(C_3)^2$	S_h	S_3	$(S_h)^2$
A'	1	1	1	1	1	1
	1	e	e*	1	e	e*
E'	1	e*	e	1	e*	e
A''	1	1	1	-1	-1	-1
	1	e	e*	-1	-e	-e*
E''	1	e*	e	-1	-e*	-e

C_3N_4 in hexagonal structure are presented in table 6.10. . Using the selection rule, the infrared active modes emanate from the A_2'' and E' modes, while the Raman active modes emerge from the A_2' and E'' modes. The Raman inactive and infrared inactive frequencies will only appear in A_2'' modes. It is worth noting that the primes and double primes are attached letters to indicate those which are, respectively, symmetric and antisymmetric with respect to σ_h. Moreso, the the subscripts 1 and 2 are attached to letters A's, B's and T's designate those which are respectively, symmetric and antisymmetric with respect to a C_2 perpendicular to the principal axis [**?**].

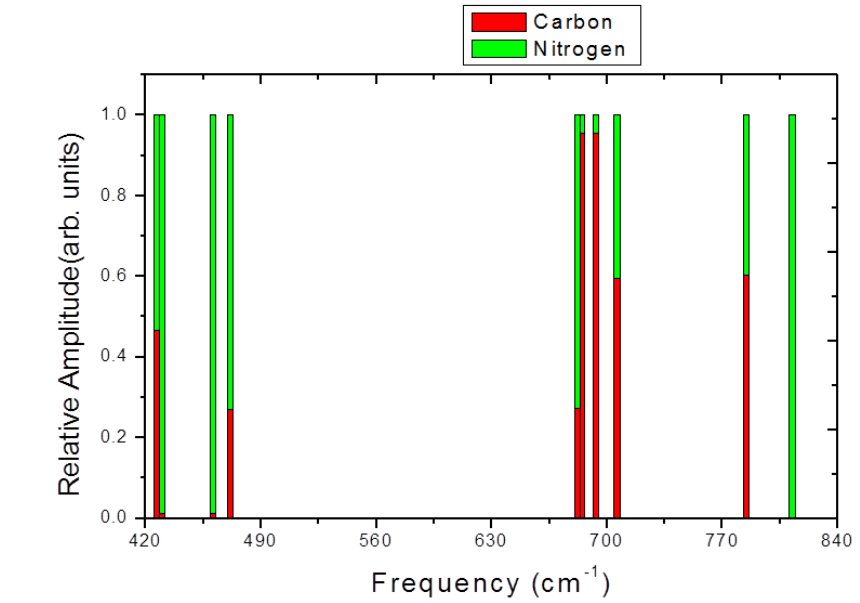
Figure 6.7 shows the infrared spectrum of C_3N_4 in hexagonal structure

From experimental point of view, a typical Raman spectrum of the graphitic C_3N_4 show two main bands at 1357 cm^{-1} and 1560 . These bands are similar to the D(1357 cm^{-1}) and G (1560 cm^{-1}) bands found in disordered graphite [26]. In these calculation the lowest infrared active modes is found at about 42 cm^{-1}

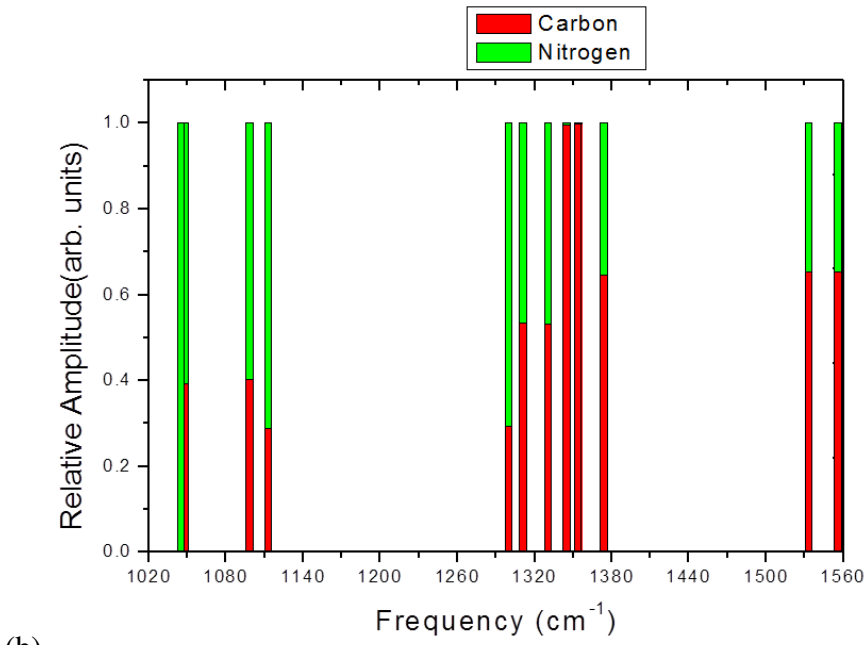
Table 6.10 Calculated vibrational frequencies of graphitic-C_3N_4, space group P_{6m2} with tentative symmetry assignments. The frequencies are given in cm^{-1}.

	This work	Others [23]
Raman		
A_1'	1047	1061
A_1'	1044	1057
		1375, 1391
E''	258^i	258.5^i
E''	237^i	231.3^i
E''	706	702
Infrared		
A_2''	132	131.5
A_2''	461	467.9
A_2''	471	474.2
A_2''	784	
A_2''	812	800.2, 830.1
E'	42	54.9
E'	681	684
E'	693	698.4, 700.6
E'	1098	1098.3
E'	1112	1112.6
E'	1299	1323.2
E'	1330	1330.5
E'	1533	1540.4
E'	1555	1560
Silent		
A_2'	426	436.4
A_2'	430	442.8
A_2'	1330	1329.8
A_2'	1344	1341.7

and 132 cm^{-1} compared to 54 cm^{-1} and 131.5 cm^{-1} obtained by Rignanese *et al* [23]. Note that the accuracy of Raman active modes predicted in these calculations agree well with theoretical work [23]. For instance, an E vibrational mode at 706 cm^{-1} is in excellent agreement with 702cm^{-1}. However, some experimental work [26] reports an active Raman E vibration at 988 cm^{-1} and not at around 706cm^{-1}. This big deviation can be attributed to existences of several polymorphs of graphitic C_3N_4.



(a)



(b)

Figure 6.7 The vibrational spectrum of graphitic C_3N_4 in hexagonal structure. The contributions of carbon and nitrogen atoms to the relative amplitudes of each vibrational frequencies are labeled in colour. Figures (a) and (b) show frequencies below and above 1000 cm^{-1} respectively.

The graphitic C_3N_4 in rhombohedral structure belongs to point group C_3v. For almost all vibrational frequencies the carbon and nitrogen atoms are involved in the contribution to the relative amplitudes except for vibration about 800 cm^{-1} and

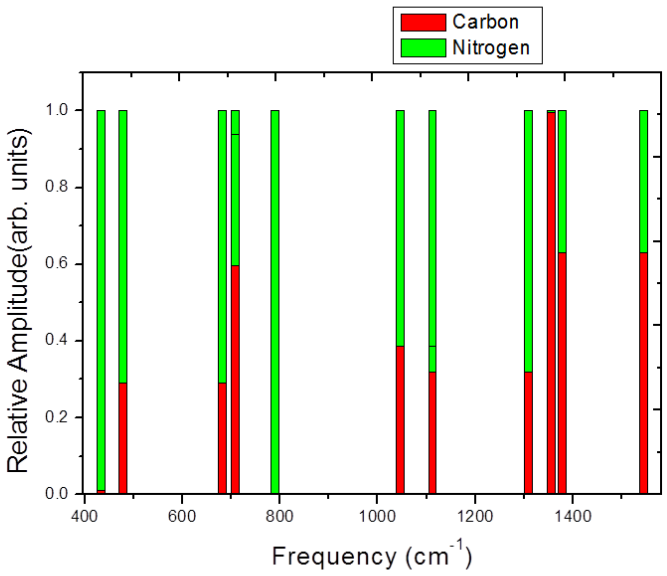


Figure 6.8 The vibrational spectra of C_3N_4 in rhombohedral structure . The contributions of carbon and nitrogen atoms to the relative amplitudes of each vibrational frequencies are labeled in colour.

1354 cm^{-1} which are associated nitrogen and carbon respectively. as shown in figure 6.8. A summary of vibrational frequencies is given in table 6.12. Table 6.11 shows characters of the irreducible representations of point group C_3v.

Table 6.11 Characters of the irreducible representations of point group C_3v for rhombohedral structure of C_3N_4. The A modes are nondegenerate while E modes are doubly degenerate.

	E	$2C_3$	$3\sigma_v$
A_1	1	1	1
A_2	1	1	-1
E	2	-1	0

Applying the selection rule, A_1 and E symmetry vibrations are infrared active. Furthermore the A_1, and E symmetry vibrations are Raman active. The A_2 symmetry vibrations are silent. From table 6.12, the calculated frequencies from VASP

code and Quantum ESPRESSO code show very small deviations of less than 5 percent. This deviations can be understood since I used plane argumentend waves potentials in VASP and ultrasoft pseudopotential in Quantum ESPRESSO.

Table 6.12 Calculated phonon frequencies of rhombohedral C_3N_4 using VASP. The frequencies are given in cm^{-1}.

Infrared active	QE	VASP
A_1	487	477
A_1	785	789
A_1	1021	1045
A_1	1320	1377
A_1	5.1^i	
E	5.9^i	
E	188^i	238^i
E	668	681
E	707	707
E	1026	
E		1112
E	1244	
E	1475	
E		1308
E		1545
Silent		
A_2	434	433
A_2	1253	
A_2		1354

In this calculation, the infrared vibration frequency graphitc C_3N_4 for rhombohedral structure range from 477 cm^{-1} to 1545 cm^{-1} based on VASP results. Notice again that an E vibrational frequencies at 1545 cm^{-1} is close to 1560 cm^{-1}, a signature of any graphitic phase of C_3N_4. A summary of vibrational frequencies for graphitic C_3N_4 in orthorhombic structure are shown in table 6.13.

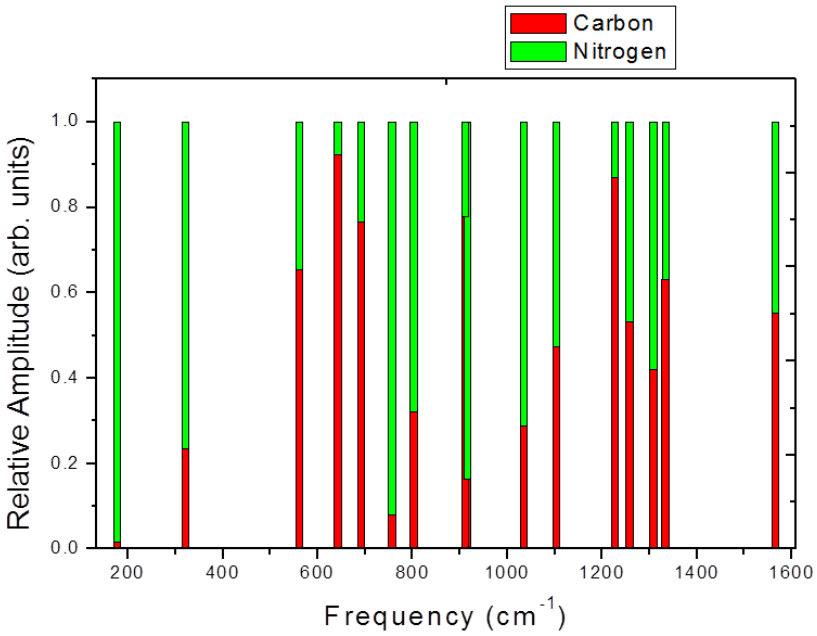


Figure 6.9 The vibration frequencies of C_3N_4 in orthorhombic structure. The contributions of carbon and nitrogen atoms to the relative amplitudes of each vibrational frequencies are labeled in colour.

Table 6.13 Calculated phonon frequencies of Orthorhombic C_3N_4 using VASP. The frequencies are given in cm^{-1} and imaginary modes are presented as i.

Infrared active	Frequencies
	177
	322
	689
	755
	897
	914
Silent	
	1576
	1564
	1314
	1301
	1254
	1229
	1094
	1031
	802
	640
	559
	67^i
	$226\ ^i$

Chapter 7

Conclusions

The results reported in this dissertation are based on first principles calculations. The focus has been directed on the structural and elastic properties of three cubic and three graphitic phases of C_3N_4. The lattice parameters agree very well with other density functional theory calculations. The bulk moduli of super-hard phases are either close or larger than that of diamond. The shear moduli on the other hand, are smaller than that of diamond. This is indicates that C_3N_4 compounds are not harder than diamond in contrast to what has been speculated earlier. Therefore, the search for a material harder than diamond is not over, yet. As the search continues, their must be emphasis on the shear rather than bulk moduli.

The elastic constants reported in this dissertation indicate that the super-hard phases (with cubic structure) have large independent elastic constants. This supports the general argument that a superhard material should have large elastic constants. Graphitic phases of C_3N_4 are harder along the a axis, and soft along the c axis.The superhard phases are stiff, as indicated by its large Young modulus. The ductility

and brittleness tests show that these material are brittle, because their low Poison's ratio which is below 0.33.

It is crucial to point out that the three graphitic phases of C_3N_4 show high frequencies close to 1560 cm^{-1} which, as noted earlier, corresponds to G band in graphite. These high frequencies are as a result of the strong C-N bonds in which the carbon atom form the sp^2 bonding [23]. Though there are similarities in graphitic C_3N_4, the Raman and infrared spectroscopy can be used to characterize these structures. In addition both crystalline superhard phases and graphitic phases of C_3N_4 can be clearly distinguished from each other due high vibrational frequencies found in graphitic phases.

7.1 Recommendation for Further Work

Layered nitride materials in the form of C_3N_4 may have other potential applications, besides their applications as precursors for superhard materials. It has been noted that graphite-like structures act as a metal-free catalyst for decomposition of harmful nitrogen oxide [147]. This field is still open, since little is known about the dielectric properties, band gap energy among other optical properties of the graphite-like structures. It will also be interesting to investigate both elastic and optical properties graphitic C_3N_4 doped with noble metals like gold and platinum. Furthermore, C_3N_4 compounds may provide a remedy for solving the global energy crisis. The layered C_3N_4 nitride is a particular semiconductor that may be seen as a photocatalyst for the splitting of hydrogen gas from water thus harvesting solar energy [148].

Appendix A

Convergence Test

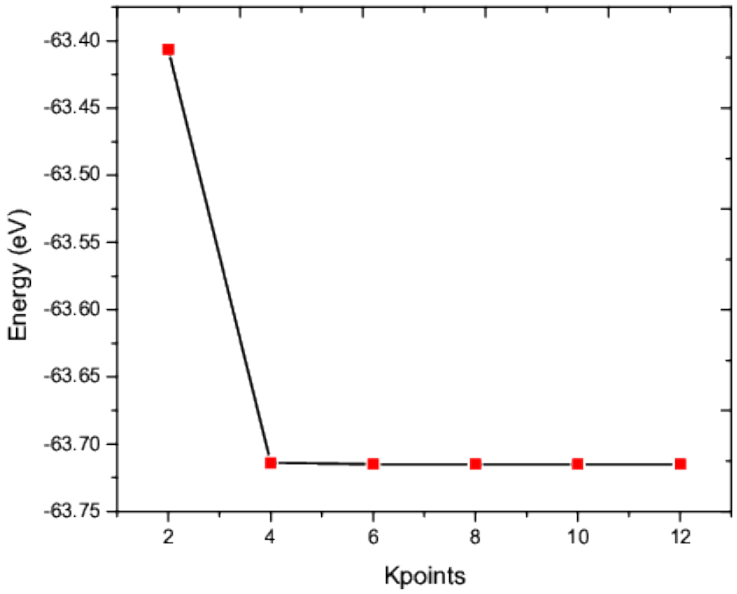


Figure 7.1 Total energy versus kpoints for defect zinc-blende-C_3N_4.

Appendix B

Estimation of hardness (Bulk modulus) using empirical model

Using an empirical expression (shown in equation 7.1) as proposed by references [5, 35, 149], we calculated the bulk modulus B as presented in Table 7.1 according to

$$B = N_c \frac{(1971 - 220\lambda)}{4d^{3.5}} \tag{7.1}$$

here N_c is the average coordination number, while d is the bond length measured in Angstroms and λ is the ionicity parameter respectively. It is assumed that N_c=4 and λ=0.5 for C_3N_4 structures, and the λ=0 for diamond. The calculated bond lengths d (C-C for diamond and C-N for C_3N_4) were extracted from Table 6.4

Table 7.1 Bulk modulus B (GPa) obtained by empirical method.

Z	Space group	B (present)	B (others)
Diamond	F_{d-3m}	425	442[c],459[h]
ZB- C_3N_4	P_{-43m}	490	430[a], 425[d]
Cubic- C_3N_4	I_{-43d}	500	480[a], 496[e]
Spinel- C_3N_4	F_{d-3m}	439	369[b], 415[f]

[a]Reference [119],
[b]Reference [120]
[c]Reference [35],
[d]Reference [25]
[e]Reference [20],
[f]Reference [121]
[h]Reference [123]

Hierarchy of hardness

Table 7.2 Hierarchy of hardness.

Hierarchy	Rank	Knoop(kg mm^{-2})	Examples
Ultrasoft	<5	<32	graphite, salt, lead, talc
Soft	5-8	32-25	silver, copper
Normal	8-10	256-1024	glass, steel
Hard	10-12	1024-4096	silicon carbide, tungsten carbide
Superhard	>12	>4096	cubic boron nitride, diamond

Reference [14]

Appendix C

Point Group

Table 7.3 Characters of the irreducible representations of point group O_h(m-3m) corresponding to diamond.

	E	$8C_3$	$6C_2$'	$6C_4$	$3C_2$	i	6S4	8S6	$3s_h$	$6s_d$
A_1g	1	1	1	1	1	1	1	1	1	1
A_2g	1	1	-1	-1	1	1	-1	1	1	-1
E_g	2	-1	0	0	2	2	0	-1	2	0
T_1g	3	0	-1	1	-1	3	1	0	-1	-1
T_2g	3	0	1	-1	-1	3	-1	0	-1	1
A_1u	1	1	1	1	1	-1	-1	-1	-1	-1
A_2u	1	1	-1	-1	1	-1	1	-1	-1	1
E_u	2	-1	0	0	2	-2	0	1	-2	0
T_1u	3	0	-1	1	-1	-3	-1	0	1	1
$T4_2u$	3	0	1	-1	-1	-3	1	0	1	-1

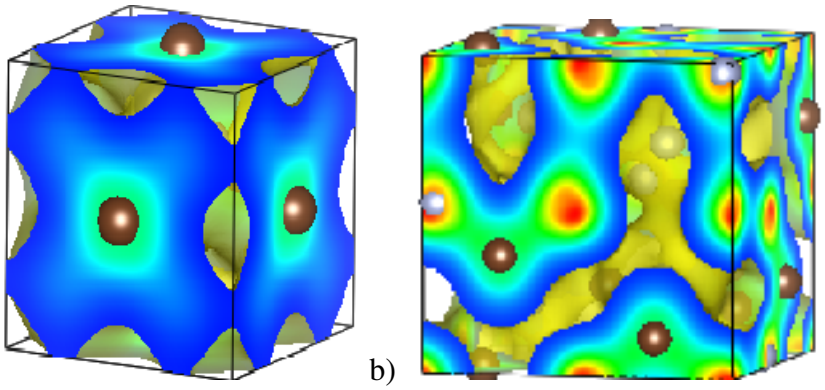
Table 7.4 Characters of the irreducible representations of point group D_3h (-62m) corresponding to graphite.

	E	2C3	3C2	s_h	2S3	$3s_v$
A_1'	1	1	1	1	1	1
A_2'	1	1	-1	1	1	-1
E'	2	-1	0	2	-1	0
A_1''	1	1	1	-1	-1	-1
A_2''	1	1	-1	-1	-1	1
E''	2	-1	0	-2	1	0

Appendix E

Charge density

Calculated charge density distribution in C_3N_4 polymorph as shown in figures 7.2 and 7.3. Throught this work, details of the charge distribution for carbon and nitrogen are not discussed. However, the charge density provides useful information about bonding in different structures.



a) b)

Figure 7.2 The charge distribution in (a) defective zinc-blende-C_3N_4, (b) cubic-C_3N_4.

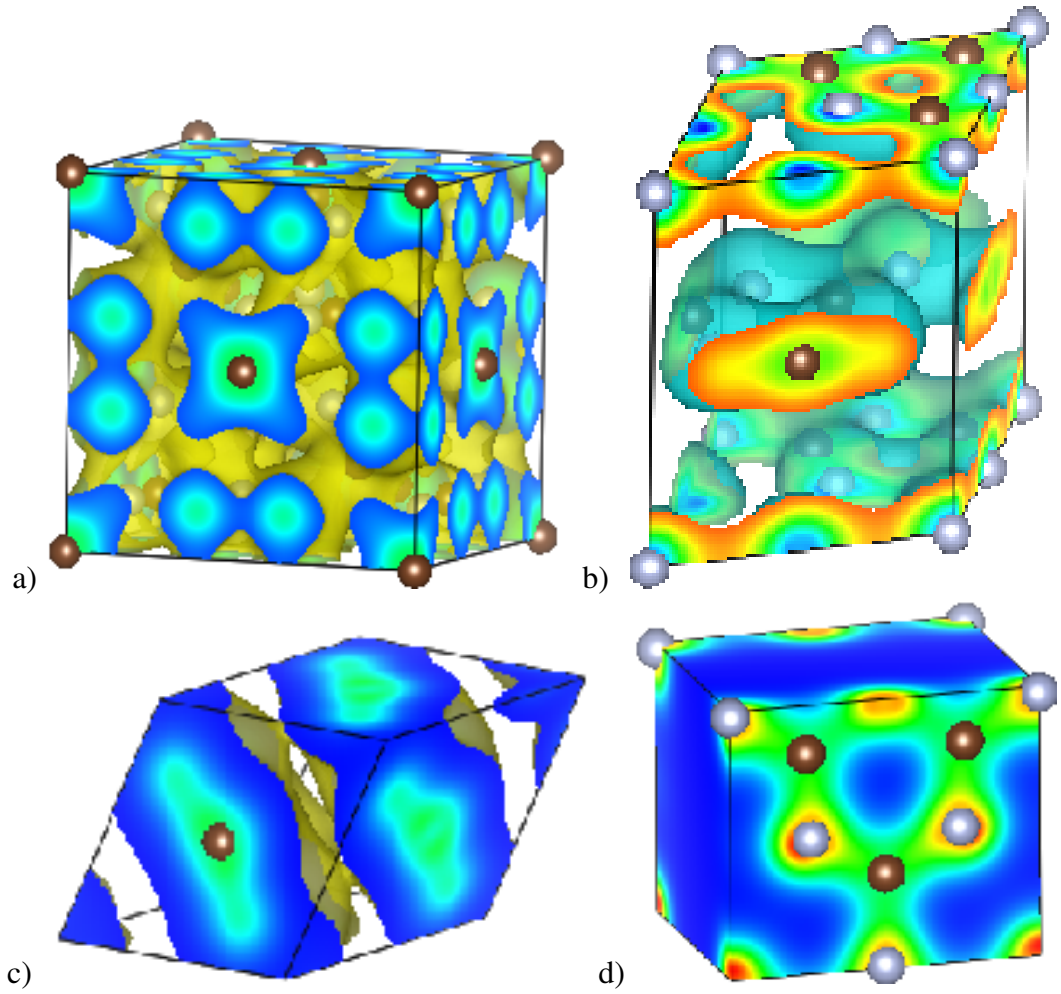


Figure 7.3 The charge distribution in (a) cubic spinel-C_3N_4(b) g-C_3N_4 (hexagonal) (c) g-C_3N_4 (rhombohedral) (d) g-C_3N_4 (orthorhombic).

Conferences and Workshops

1. G. S. Manyali and J. E. Lowther, Ab-initio study of elastic properties of super hard and graphitic structures of C_3N_4 (DST/NRF Center of Excellence in Strong Materials Annual Workshop, Johannesburg, April, 2011) [Poster Presentation].

Bibliography

[1] O. Kurakevych, Journal of Superhard Materials 31 (3) (2009) 139–157.

[2] M. Mattesini, S. Matar, Computational materials science 20 (1) (2001) 107–119.

[3] D. Tabor, Proceedings of the Physical Society. Section B 67 (1954) 249.

[4] D. Tabor, Oxford University Press, USA, 2000.

[5] A. Liu, M. Cohen, Science 245 (4920) (1989) 841.

[6] A. Gerk, Journal of Materials Science 12 (4) (1977) 735–738.

[7] M. Hebbache, Solid state communications 113 (8) (2000) 427–432.

[8] F. Gao, J. He, E. Wu, S. Liu, D. Yu, D. Li, S. Zhang, Y. Tian, Physical review letters 91 (1) (2003) 15502.

[9] A. Bosak, M. Krisch, M. Mohr, J. Maultzsch, C. Thomsen, Phys. Rev. B 75 (15) (2007) 153408.

[10] A. Oganov, Boron Rich Solids (2011) 207–225.

[11] J. Lowther, Boron Rich Solids (2011) 131–145.

[12] G. Goglio, D. Foy, G. Demazeau, Materials Science and Engineering R Reports 58 (6) (2008) 195–227.

[13] J. Leger, J. Haines, Endeavour 21 (3) (1997) 121–124.

[14] C. Sung, M. Sung, Materials chemistry and physics 43 (1) (1996) 1–18.

[15] K. Li, D. Xue, Physica Scripta Volume T 139 (1) (2010) 014073–+.

[16] P. McMillan, Current Opinion in Solid State and Materials Science 4 (2) (1999) 171–178.

[17] V. Khabashesku, J. Zimmerman, J. Margrave, Chemistry of materials 12 (11) (2000) 3264–3270.

[18] W. R. Liu, A.Y., Physical Review B 50 (14) (1994) 10362–10365.

[19] C. M. Liu, A.Y., Physical Review B 41 (15) (1990) 10727–10734.

[20] H. R. Teter, D.M., Science 271 (5245) (1996) 53–55.

[21] J. Lowther, Physical Review B - Condensed Matter and Materials Physics 57 (10) (1998) 5724–5727.

[22] A. Reyes-Serrato, D. Galván, I. Garzón, Physical Review B 52 (9) (1995) 6293.

[23] G. Rignanese, J. Charlier, X. Gonze, Physical Review B 66 (20) (2002) 205416.

[24] S.-D. Mo, L. Ouyang, W. Ching, I. Tanaka, Y. Koyama, R. Riedel, Physical Review Letters 83 (24) (1999) 5046–5049.

[25] A. Liu, R. Wentzcovitch, Physical Review B 50 (14) (1994) 10362.

[26] P. Zinin, L.-C. Ming, S. Sharma, V. Khabashesku, X. Liu, S. Hong, S. Endo, T. Acosta, Chemical Physics Letters 472 (1-3) (2009) 69–73.

[27] L. Ming, P. Zinin, Y. Meng, X. Liu, S. Hong, Y. Xie, Journal of Applied Physics 99 (3).

[28] I. Alves, G. Demazeau, W. F. Tanguy, B., Solid State Communications 109 (11) (1999) 697–701.

[29] H. Zhao, X. Chen, C. Jia, T. Zhou, X. Qu, J. Jian, Y. Xu, T. Zhou, Materials Science and Engineering B: Solid-State Materials for Advanced Technology 122 (3) (2005) 226–230.

[30] D. Shi, X. Zhang, L. Yuan, Y. Gu, Y. Zhang, Z. Duan, X. Chang, Z. Tian, N. Chen, Applied surface science 148 (1-2) (1999) 50–55.

[31] K. Yu, M. Cohen, E. Haller, W. Hansen, A. Liu, I. Wu, Physical Review B 49 (7) (1994) 5034.

[32] P. Moreau, F. Boucher, G. Goglio, D. Foy, V. Mauchamp, G. Ouvrard, Phys. Rev. B 73 (19) (2006) 195111.

[33] J. Badding, D. Nesting, Chemistry of materials 8 (2) (1996) 535–540.

[34] Y. Yoon, B. Pfrommer, F. Mauri, S. Louie, Physical review letters 80 (15) (1998) 3388–3391.

[35] R. Musin, D. Musaev, M. Lin, The Journal of Physical Chemistry B 103 (5) (1999) 797–803.

[36] J. Martin-Gil, F. Martin-Gil, M. Sarikaya, M. Qian, M. José-Yacamán, A. Rubio, Journal of applied physics 81 (1997) 2555.

[37] G. Goglio, D. Foy, S. Pechev, J. Majimel, G. Demazeau, N. Guignot, D. Andrault, Diamond and Related Materials 18 (4) (2009) 627–631.

[38] P. Zinin, L. Ming, I. Kudryashov, N. Konishi, S. Sharma, Journal of Raman Spectroscopy 38 (10) (2007) 1362–1367.

[39] A. Zerr, G. Miehe, G. Serghiou, M. Schwarz, E. Kroke, R. Riedel, H. Fueß, P. Kroll, R. Boehler, Nature 400 (6742) (1999) 340–342.

[40] I. Tanaka, T. Mizoguchi, T. Sekine, H. He, K. Kimoto, T. Kobayashi, S. Mo, W. Ching, Applied Physics Letters 78 (2001) 2134.

[41] W. Ching, S. Mo, L. Ouyang, I. Tanaka, M. Yoshiya, Physical Review B 61 (16) (2000) 10609.

[42] M. S.-D. T. I. Y. M. Ching, W.Y., Physical Review B - Condensed Matter and Materials Physics 63 (6) (2001) 641021–641024.

[43] J. Berryman, Journal of the Mechanics and Physics of Solids 53 (10) (2005) 2141–2173.

[44] T. Barron, M. Klein, Proceedings of the Physical Society 85 (1965) 523.

[45] M. A. Biot, Journal of Applied Physics 25 (11) (1954) 1385 –1391.

[46] F. Birch, Phys. Rev. 71 (11) (1947) 809–824.

[47] R. Hill, Journal of the Mechanics and Physics of Solids 5 (4) (1957) 229–241.

[48] E. Kroner, Journal of the Mechanics and Physics of Solids 15 (5) (1967) 319–329.

[49] J. Nye, Oxford University Press, USA, 1985.

[50] R. F. S. Hearmon, Rev. Mod. Phys. 18 (3) (1946) 409–440.

[51] A. G. Every, W. Sachse, Phys. Rev. B 42 (13) (1990) 8196–8205.

[52] R. Martin, Cambridge Univ Pr, 2004.

[53] P. Hohenberg, W. Kohn, Phys. Rev. 136 (3B) (1964) B864–B871.

[54] W. Kohn, L. J. Sham, Phys. Rev. 140 (4A) (1965) A1133–A1138.

[55] K. Ohno, K. Esfarjani, Y. Kawazoe, Vol. 129, Springer Verlag, 1999.

[56] A. Szabo, N. Ostlund, Dover Pubns, 1996.

[57] J. C. Slater, Phys. Rev. 81 (1951) 385–390.

[58] A. Becke, The Journal of Chemical Physics 98 (1993) 1372.

[59] A. Görling, M. Ernzerhof, Phys. Rev. A 51 (1995) 4501–4513.

[60] W. Kohn, A. Becke, R. Parr, The Journal of Physical Chemistry 100 (31) (1996) 12974–12980.

[61] Phys. Rev. A 54 (1996) 3912–3915.

[62] M. Levy, Proceedings of the National Academy of Sciences 76 (12) (1979) 6062.

[63] D. Feng, G. Jin, Vol. 1, World Scientific Pub Co Inc, 2005.

[64] L. Vitos, Springer Verlag, 2007.

[65] J. Galsin, Springer Us, 2002.

[66] K. Inoue, K. Ohtaka, Vol. 94, Springer Verlag, 2004.

[67] U. Mizutani, Cambridge Univ Pr, 2001.

[68] E. Wimmer, H. Krakauer, M. Weinert, A. Freeman, Physical Review B 24 (2) (1981) 864.

[69] G. Kerker, Journal of Physics C: Solid State Physics 13 (1980) L189.

[70] J. P. Perdew, A. Zunger, Phys. Rev. B 23 (10) (1981) 5048–5079.

[71] J. Perdew, K. Burke, M. Ernzerhof, Physical Review Letters 77 (18) (1996) 3865–3868.

[72] D. Ceperley, B. Alder, Physical Review Letters 45 (7) (1980) 566–569.

[73] J. Perdew, Y. Wang, Physical Review B 45 (23) (1992) 13244.

[74] T. Leung, C. Chan, B. Harmon, Physical Review B 44 (7) (1991) 2923.

[75] C. Wang, B. Klein, H. Krakauer, Physical Review Letters 54 (16) (1985) 1852–1855.

[76] M. Grüning, A. Marini, A. Rubio, The Journal of chemical physics 124 (2006) 154108.

[77] S. Lebègue, M. Klintenberg, O. Eriksson, M. Katsnelson, Physical Review B 79 (24) (2009) 245117.

[78] P. Rinke, A. Qteish, J. Neugebauer, C. Freysoldt, M. Scheffler, New Journal of Physics 7 (2005) 126.

[79] J. Perdew, J. Chevary, S. Vosko, K. Jackson, M. Pederson, D. Singh, C. Fiolhais, Physical Review B 46 (11) (1992) 6671.

[80] J. Perdew, K. Burke, M. Ernzerhof, Physical Review Letters 80 (4) (1998) 891–891.

[81] A. El-Barbary, Ph.D. thesis, University of Sussex (2005).

[82] D. Singh, L. Nordström, Springer Verlag, 2006.

[83] V. Ozoliņš, M. Körling, Phys. Rev. B 48 (1993) 18304–18307.

[84] E. Proynov, E. Ruiz, A. Vela, D. Salahub, International Journal of Quantum Chemistry 56 (S29) (1995) 61–78.

[85] M. Cohen, V. Heine, Solid state physics 24 (1970) 37–248.

[86] J. Phillips, L. Kleinman, Physical Review 116 (2) (1959) 287.

[87] G. Bachelet, D. Hamann, M. Schluter, Physical Review B 26 (8) (1982) 4199.

[88] A. Rappe, K. Rabe, E. Kaxiras, J. Joannopoulos, Physical Review B 41 (2) (1990) 1227.

[89] L. Kleinman, D. Bylander, Physical Review Letters 48 (20) (1982) 1425–1428.

[90] J. Hutter, H. Luthi, M. Parrinello, Computational Materials Science 2 (2) (1994) 244–248.

[91] D. Hamann, M. Schluter, C. Chiang, Physical Review Letters 43 (20) (1979) 1494–1497.

[92] N. Troullier, J. Martins, Physical Review B 43 (3) (1991) 1993.

[93] D. Vanderbilt, Physical Review B 41 (11) (1990) 7892.

[94] G. Kresse, D. Joubert, Phys. Rev. B 59 (1999) 1758–1775.

[95] N. Holzwarth, G. Matthews, R. Dunning, A. Tackett, Y. Zeng, Physical Review B 55 (4) (1997) 2005.

[96] P. Blöchl, Physical Review B 50 (24) (1994) 17953.

[97] H. Monkhorst, J. Pack, Physical Review B 13 (12) (1976) 5188–5192.

[98] P. Hohenberg, W. Kohn, Phys. Rev. 136 (3B) (1964) B864–B871.

[99] W. Kohn, L. J. Sham, Phys. Rev. 140 (4A) (1965) A1133–A1138.

[100] G. Kresse, D. Joubert, Phys. Rev. B 59 (3) (1999) 1758–1775.

[101] J. P. Perdew, A. Zunger, Phys. Rev. B 23 (10) (1981) 5048–5079.

[102] G. Kresse, J. Hafner, Physical Review B 47 (1) (1993) 558.

[103] G. Kresse, J. Hafner, Phys. Rev. B 49 (20) (1994) 14251–14269.

[104] G. Kresse, J. Furthmuller, Computational Materials Science 6 (1) (1996) 15–50.

[105] P. Giannozzi, S. Baroni, N. Bonini, M. Calandra, R. Car, C. Cavazzoni, D. Ceresoli, G. Chiarotti, M. Cococcioni, I. Dabo, et al., Journal of Physics: Condensed Matter 21 (2009) 395502.

[106] D. Hobbs, G. Kresse, J. Hafner, Physical Review B 62 (17) (2000) 11556.

[107] G. Kresse, O. Lebacq, cms. mpi. u nivie. ac. at/vasp/vasp/vasp. html.

[108] J. Poirier, A. Tarantola, Physics of the Earth and Planetary Interiors 109 (1-2) (1998) 1–8.

[109] O. Anderson, Vol. 31, 1995.

[110] A. Keane, Australian Journal of Physics 7 (2) (1954) 322–333.

[111] R. Jeanloz, Physical Review B 38 (1) (1988) 805.

[112] P. Vinet, J. Ferrante, J. Rose, J. Smith, Journal of Geophysical Research 92 (B9) (1987) 9319–9325.

[113] F. Murnaghan, Proceedings of the national academy of sciences of the United States of America 30 (9) (1944) 244.

[114] F. Murnaghan, American Journal of Mathematics 59 (2) (1937) 235–260.

[115] F. Birch, Journal of Geophysical Research 83 (B3) (1978) 1257–1268.

[116] F. Tuinstra, J. Koenig, The Journal of Chemical Physics 53 (1970) 1126.

[117] D. Chung, Journal of materials science 37 (8) (2002) 1475–1489.

[118] D. Roundy, M. L. Cohen, Phys. Rev. B 64 (21) (2001) 212103.

[119] J. Martin-Gil, F. Martin-Gil, M. Sarikaya, M. Qian, M. Jos-Yacamn, A. Rubio, Journal of Applied Physics 81 (6) (1997) 2555–2559.

[120] S.-D. Mo, L. Ouyang, W. Y. Ching, I. Tanaka, Y. Koyama, R. Riedel, Phys. Rev. Lett. 83 (24) (1999) 5046–5049.

[121] P. Mori-Sánchez, M. Marqués, A. Beltrán, J. Z. Jiang, L. Gerward, J. M. Recio, Phys. Rev. B 68 (6) (2003) 064115.

[122] M. Marqués, J. Osorio, R. Ahuja, M. Flórez, J. Recio, Physical Review B 70 (10) (2004) 104114.

[123] Y. Zhang, H. Sun, C. Chen, Physical Review B 73 (6) (2006) 064109.

[124] F. Birch, Physical Review 71 (11) (1947) 809.

[125] G. Pradhan, A. Kumar, S. Deb, U. Waghmare, C. Narayana, Physical Review B 82 (14) (2010) 144112.

[126] J. Zhao, C. Fan, Physica B: Condensed Matter 403 (10-11) (2008) 1956–1959.

[127] N. Mounet, N. Marzari, Physical Review B 71 (20) (2005) 205214.

[128] Z. Sun, R. Ahuja, J. Lowther, Solid State Communications 150 (15-16) (2010) 697–700.

[129] M. Born, K. Huang, Oxford University Press, USA, 1998.

[130] R. Hill, Proceedings of the Physical Society. Section A 65 (1952) 349.

[131] A. Reuss, Z. Angew. Math. Mech 9 (1929) 49–58.

[132] Q. Liu, Z. Liu, L. Feng, physica status solidi (b).

[133] S. Lee, D. Bylander, L. Kleinman, Physical Review B 45 (1992) 3245–3247.

[134] J. Haines, J. Leger, G. Bocquillon, Annual Review of Materials Research 31 (1) (2001) 1–23.

[135] S. Pugh, Philosophical Magazine Series 7 45 (367) (1954) 823–843.

[136] M. Starfield, A. Shrager, New York, McGraw-Hill, 1972.

[137] G. Kresse, J. Furthmuller, J. Hafner, EPL (Europhysics Letters) 32 (1995) 729.

[138] J. Gilman, Cambridge Univ Pr, 2003.

[139] B. Karki, L. Stixrude, R. Wentzcovitch, Rev. Geophys 39 (4) (2001) 507–534.

[140] P. Lespade, A. Marchand, M. Couzi, F. Cruege, Carbon 22 (4-5) (1984) 375–385.

[141] A. Ferrari, J. Robertson, Physical Review B 61 (20) (2000) 14095.

[142] F. Rice, E. Teller, K. Hedberg, The Journal of Physical Chemistry 53 (8) (1949) 1308–1308.

[143] G. Burns, Academic Press, Inc., New York, 1977.

[144] A. Ferrari, S. Rodil, J. Robertson, Physical Review B 67 (15) (2003) 155306.

[145] A. Vincent, Wiley, 1977.

[146] J. Kaufman, S. Metin, D. Saperstein, Physical Review B 39 (18) (1989) 13053.

[147] J. Zhu, Y. Wei, W. Chen, Z. Zhao, A. Thomas, Chemical Communications 46 (37) (2010) 6965–6967.

[148] S. Yan, Z. Li, Z. Zou, Langmuir 26 (6) (2010) 3894–3901.

[149] M. Cohen, Materials Science and Engineering: A 209 (1-2) (1996) 1–4.